Eur. Phys. J. A (2015) **51**: 24
DOI 10.1140/epja/i2015-15024-1

THE EUROPEAN PHYSICAL JOURNAL A

Regular Article – Theoretical Physics

Subtracted dispersion relation formalism for the two-photon exchange correction to elastic electron-proton scattering: Comparison with data

O. Tomalak[1,2,3,a] and M. Vanderhaeghen[1,2]

[1] Institut für Kernphysik, Johannes Gutenberg Universität, Mainz, Germany
[2] PRISMA Cluster of Excellence, Johannes Gutenberg-Universität, Mainz, Germany
[3] Department of Physics, Taras Shevchenko National University of Kyiv, Kyiv, Ukraine

Received: 22 January 2015
Published online: 27 February 2015 – © Società Italiana di Fisica / Springer-Verlag 2015
Communicated by M. Anselmino

Abstract. We apply a subtracted dispersion relation formalism with the aim to improve predictions for the two-photon exchange corrections to elastic electron-proton scattering observables at finite momentum transfers. We study the formalism on the elastic contribution, and make a detailed comparison with existing data for unpolarized cross sections as well as polarization transfer observables.

1 Introduction

Lepton scattering within the one-photon exchange approximation is a time-honored tool to access information on the internal structure of hadrons, in particular the distribution of charge and magnetization within a nucleon. The traditional way to access nucleon form factors (FFs) —the Rosenbluth separation technique— measures the angular dependence of the unpolarized differential cross section for elastic electron-nucleon scattering. Electric and magnetic FFs have been measured with this technique, see refs. [1, 2] for such recent state-of-the-art measurements, and, *e.g.*, ref. [3] for a review of older data. The development of the recoil polarization technique as well as the availability of polarized targets at electron scattering facilities led to the possibility of a second method of FF measurements. Such experiments access the ratio G_E/G_M of electric (G_E) to magnetic (G_M) FFs directly from the ratio of the transverse to longitudinal nucleon polarizations in elastic electron-nucleon scattering. For squared momentum transfers Q^2 up to $8.5\,\mathrm{GeV}^2$, this ratio has been measured at Jefferson Laboratory (JLab) in a series of experiments [4–7], with projects to extend these measurements in the near future at the JLab 12 GeV facility to even larger Q^2 values [8]. It came as a surprise that the two experimental approaches to access nucleon FFs, assuming the single-photon exchange approximation, gave strikingly different results for the FF ratio, for Q^2 value above $1.0\,\mathrm{GeV}^2$. Two-photon exchange (TPE) processes have been proposed as a plausible solution to resolve this puzzle [9,10], see ref. [11] for a review. Estimates for TPE processes were studied in a variety of different model calculations, see, *e.g.*, refs. [9, 12–21], and first phenomenological extractions of TPE observables based on available data were given, see, *e.g.*, refs. [22–27]. Furthermore, dedicated experiments to directly measure the TPE observables have been performed in recent years [28, 29], or are underway [30, 31].

Besides electron scattering experiments, information on the proton size can also be obtained from atomic spectroscopy. Theoretical predictions for the hydrogen spectrum within QED are performed to such accuracy that they can be used as a precision tool to extract the proton radius, see, *e.g.*, ref. [32] for a recent work and references therein. It came as a surprise that the recent extractions of the proton charge radius from muonic hydrogen Lamb shift measurements [33,34] are in strong contradiction, by around 7 standard deviations, with the values obtained from energy level shifts in electronic hydrogen or from electron-proton scattering experiments. This so-called "proton radius puzzle" has triggered a large activity and is the subject of intense debate, see, *e.g.*, refs. [35, 36] for recent reviews. The limiting accuracy in extracting the proton charge radius from the Lamb shift measurements in muonic atoms is due to hadronic corrections. Among these, the leading uncertainty originates from the so-called polarizability correction, which corresponds with a TPE process between the lepton and the proton. This correction can be obtained from the knowledge of forward double virtual Compton structure amplitudes, which has been estimated from phenomenology [37–40], from nonrelativistic QED effective field theory [41], as well as from

[a] e-mail: tomalak@uni-mainz.de

chiral effective field theory [42–45]. The total TPE corrections to the Lamb shift were found to be in the 10–15% range of the total discrepancy for the proton charge radius extractions between electron scattering and muonic atom spectroscopy. Although these TPE corrections are not large enough to explain the bulk of the difference between both extraction methods, they constitute a large hadronic correction to the Lamb shift result, which needs to be taken into account as accurately as possible when extracting the proton radius from such experiments.

The "proton radius puzzle" also calls for revisiting the TPE corrections in the elastic electron-nucleon scattering data in the low-Q^2 region, from which the proton radius is obtained. In the low Q^2 region we expect the main contribution to TPE corrections from the elastic intermediate state. Its leading contribution is given by the Coulomb scattering of relativistic electrons off the proton charge distribution, and was obtained by McKinley and Feshbach [46]. Although the corrections to the Coulomb distortion in elastic electron-proton scattering were found to be small in the small Q^2 region [47], a high-precision extraction of the proton radii, especially its magnetic radius, calls for an assessment of the model dependence of the TPE corrections.

In this work we aim to revisit the TPE corrections in the region of low Q^2 up to about $1\,\mathrm{GeV}^2$, and make a detailed comparison with the available data. In this work, we will focus our study on the elastic contribution of the TPE correction to the unpolarized elastic electron-proton scattering cross section. Two main calculations have been developed in the literature to estimate this elastic TPE contribution. A first method of calculation, performed by Blunden, Melnitchouk, and Tjon [9] evaluates the two-photon box graph with the assumption of on-shell virtual photon-proton-proton vertices. A second method of calculation, performed by Borisyuk and Kobushkin [16], evaluates this elastic TPE correction within unsubtracted dispersion relations (DRs). In this work we compare these two methods and compare them in detail to the recent data. In order to minimize the model dependence due to unknown or poorly constrained contributions from higher intermediate states, we propose a DR approach with one subtraction, where the subtraction constant, which encodes the less well constrained physics at high energies, is fitted to the available data.

The paper is organized as follows: We describe the general formalism of elastic electron-proton scattering in the limit of massless electrons in sect. 2. We review the DR framework in sect. 3: we subsequently discuss how to obtain the imaginary parts of the TPE amplitudes from unitarity relations in the physical region, their analytical continuation to the unphysical region, as well as how to reconstruct the real parts using dispersive integrals. We review the two-photon box graph model evaluation with the assumption of an on-shell form of virtual photon-proton-proton vertex in sect. 4: we subsequently discuss the loop diagram evaluation of the box graph, as well as its dispersive evaluation. We also discuss the forward limit and provide an analytical formula which describe the leading corrections beyond the Feshbach Coulomb correction formula. In sect. 5, we make detailed comparisons between both methods, and show that a subtraction eliminates the differences between both methods. Using such a subtracted DR formalism for the TPE contribution, we provide a detailed study of available unpolarized and polarized elastic electron-proton scattering datafor the case of the elastic intermediate state. We present our conclusions and outlook in sect. 6. Some technical details on unitarity relations and on the integrals entering the box diagram are collected in three appendices.

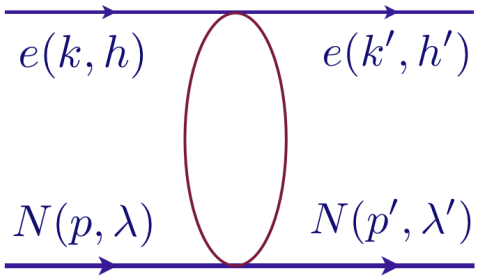

Fig. 1. Elastic electron-proton scattering.

2 Elastic electron-proton scattering in the limit of massless electrons

Elastic electron-proton scattering $e(k,h) + p(p,\lambda) \to e(k',h') + p(p',\lambda')$, where $h(h')$ denote the incoming (outgoing) electron helicities and $\lambda(\lambda')$ the corresponding proton helicities respectively, (see fig. 1), is completely described by 2 Mandelstam variables, *e.g.*, $Q^2 = -(k-k')^2$ —the squared momentum transfer— and $s = (p+k)^2$ — the squared energy in the electron-proton center-of-mass (c.m.) reference frame.

It is convenient to introduce the average momentum variables $P = (p+p')/2$, $K = (k+k')/2$, the u-channel squared energy $u = (k-p')^2$, and the crossing symmetry variable $\nu = (s-u)/4$ which changes sign under $s \leftrightarrow u$ channel crossing. Instead of the Mandelstam invariant s or the crossing symmetric variable ν, it is customary in experiment to use the virtual photon polarization parameter ε, which varies between 0 and 1, indicating the degree of the longitudinal polarization in case of one-photon exchange. We will be working in the limit of ultra-relativistic electrons, allowing to neglect the electron mass. In terms of Q^2 and ν, ε is then defined as

$$\varepsilon = \frac{16\nu^2 - Q^2(Q^2+4M^2)}{16\nu^2 + Q^2(Q^2+4M^2)}\,, \tag{1}$$

where M denotes the proton mass.

It is convenient to work in the c.m. reference frame with electron scattering angle θ_{cm}. The momentum transfer is then given by $Q^2 = \frac{(s-M^2)^2}{s}\sin^2\frac{\theta_{\mathrm{cm}}}{2}$.

There are 16 helicity amplitudes $T_{h'\lambda',h\lambda}$ with arbitrary $h,h',\lambda,\lambda' = \pm 1/2$ in, but discrete symmetries of QCD and QED leave just six independent amplitudes. The momentum transfer accessed by current experiments down

to $Q^2 \gtrsim 0.001\,\mathrm{GeV}^2$ [1, 2] is still much larger than the squared electron mass, so that to very good approximation electrons can be treated as massless particles. As all amplitudes with electron helicity flip are suppressed by the electron mass, in the limit of massless electrons only three independent helicity amplitudes survive: $T_1 \equiv T_{\frac{1}{2}\frac{1}{2},\frac{1}{2}\frac{1}{2}}$, $T_2 \equiv T_{\frac{1}{2}-\frac{1}{2},\frac{1}{2}\frac{1}{2}}$, $T_3 \equiv T_{\frac{1}{2}-\frac{1}{2},\frac{1}{2}-\frac{1}{2}}$.

The helicity amplitude for elastic $e^- p$ scattering can be expressed through three independent tensor structures. It is common to use the following notations [10]:

$$T = \frac{e^2}{Q^2}\bar{u}(k',h)\gamma_\mu u(k,h)\cdot\bar{u}(p',\lambda') \times\left(\mathcal{G}_M\gamma^\mu - \mathcal{F}_2\frac{P^\mu}{M} + \mathcal{F}_3\frac{\gamma.KP^\mu}{M^2}\right)u(p,\lambda), \quad (2)$$

where the structure amplitudes $\mathcal{G}_M$, $\mathcal{F}_2$, $\mathcal{F}_3$ are functions of ν and Q^2.

Following the Jacob-Wick [48] phase convention, the three independent helicity amplitudes can be expressed through the structure amplitudes as

$$\begin{aligned} T_1 &= \frac{2e^2}{Q^2}\left\{\frac{su-M^4}{s-M^2}\left(\mathcal{F}_2-\mathcal{G}_M-\frac{s-M^2}{2M^2}\mathcal{F}_3\right)+Q^2\mathcal{G}_M\right\},\\ T_2 &= -\frac{e^2}{Q^2}\frac{\sqrt{Q^2(M^4-su)}}{M}e^{-i\phi} \times\left\{\mathcal{F}_2+2\frac{M^2}{s-M^2}\left(\mathcal{F}_2-\mathcal{G}_M\right)-\mathcal{F}_3\right\},\\ T_3 &= 2\frac{e^2}{Q^2}\frac{su-M^4}{s-M^2}\left\{\mathcal{F}_2-\mathcal{G}_M-\frac{s-M^2}{2M^2}\mathcal{F}_3\right\}, \end{aligned} \quad (3)$$

where ϕ is the azimuthal angle of the scattered electron. Notice that following the Jacob-Wick phase convention, the azimuthal angular dependence of the helicity amplitudes is in general given by $T_{h'\lambda',h\lambda} = e^{i(\Lambda-\Lambda')\phi}$, with $\Lambda = h-\lambda$ and $\Lambda' = h'-\lambda'$.

The structure amplitudes can in turn be expressed through the helicity amplitudes as [49]

$$\begin{aligned} \mathcal{G}_M &= \frac{1}{2}\left\{\tilde{t}_1-\tilde{t}_3\right\},\\ \mathcal{F}_2 &= \frac{MQ}{\sqrt{M^4-su}}\left\{-\tilde{t}_2e^{i\phi}+\tilde{t}_3\frac{MQ}{\sqrt{M^4-su}}\right\},\\ \mathcal{F}_3 &= \frac{M^2}{s-M^2}\left\{-\tilde{t}_1-\tilde{t}_2\frac{2MQ}{\sqrt{M^4-su}}e^{i\phi} +\tilde{t}_3\left(1+Q^2\frac{s+M^2}{M^4-su}\right)\right\}, \end{aligned} \quad (4)$$

with $\tilde{t} = T/e^2$.

In the one-photon (1γ) exchange approximation the helicity amplitude for elastic $e^- p$ scattering can be expressed in terms of the Dirac F_1 and Pauli F_2 FFs as

$$T = \frac{e^2}{Q^2}\bar{u}(k',h)\gamma_\mu u(k,h)\cdot\bar{u}(p',\lambda') \times\left(\gamma^\mu F_1(Q^2)+\frac{i\sigma^{\mu\nu}q_\nu}{2M}F_2(Q^2)\right)u(p,\lambda). \quad (5)$$

When extracting FFs from experiment, it is useful to introduce Sachs magnetic and electric FFs

$$G_M = F_1+F_2, \qquad G_E = F_1-\tau F_2, \quad (6)$$

with $\tau = Q^2/(4M^2)$.

In the one-photon exchange approximation, the structure amplitudes defined in eq. (2) can be expressed in terms of the FFs as: $\mathcal{G}_M = G_M(Q^2)$, $\mathcal{F}_2 = F_2(Q^2)$, $\mathcal{F}_3 = 0$. The exchange of more than one photon gives corrections to all amplitudes $\mathcal{G}_M$, $\mathcal{F}_2$, $\mathcal{F}_3$, which we denote by

$$\begin{aligned} \mathcal{G}_M^{2\gamma} &\equiv \mathcal{G}_M(\nu,Q^2) - G_M(Q^2),\\ \mathcal{F}_2^{2\gamma} &\equiv \mathcal{F}_2(\nu,Q^2) - F_2(Q^2),\\ \mathcal{F}_3^{2\gamma} &\equiv \mathcal{F}_3(\nu,Q^2). \end{aligned} \quad (7)$$

In the following, we consider the correction to observables due to TPE which are corrections of order e^2. The correction to the unpolarized elastic electron-proton cross section is given by the interference between the 1γ-exchange diagram and the sum of box and crossed-box diagrams with two photons. Including the TPE corrections, we can express the $e^- p$ elastic cross section through the cross section in the 1γ-exchange approximation $\sigma_{1\gamma}$ by

$$\sigma = \sigma_{1\gamma}\left(1+\delta_{2\gamma}\right), \quad (8)$$

where the TPE correction $\delta_{2\gamma}$ can be expressed in terms of the TPE amplitudes as

$$\delta_{2\gamma} = \frac{2}{G_M^2+\frac{\varepsilon}{\tau}G_E^2}\left\{\left(G_M+\frac{\varepsilon}{\tau}G_E\right)\Re\mathcal{G}_M^{2\gamma} -\frac{\varepsilon(1+\tau)}{\tau}G_E\Re\mathcal{F}_2^{2\gamma}+\left(G_M+\frac{1}{\tau}G_E\right)\frac{\nu\varepsilon}{M^2}\Re\mathcal{F}_3^{2\gamma}\right\}. \quad (9)$$

The longitudinal and transverse polarization transfer observables (P_t and P_l) are also influenced by TPE. Their following ratio is measured experimentally [28]. Experimental data on longitudinal polarization transfer allows to reconstruct [28] the longitudinal polarization transfer with enough precision,

$$\frac{P_t}{P_l} = -\sqrt{\frac{2\varepsilon}{\tau(1+\varepsilon)}}\left(\frac{G_E}{G_M}+(1+\tau)\frac{F_2\Re\mathcal{G}_M^{2\gamma}-G_M\Re\mathcal{F}_2^{2\gamma}}{G_M^2} +\left(1-\frac{2\varepsilon}{1+\varepsilon}\frac{G_E}{G_M}\right)\frac{\nu}{M^2}\frac{\Re\mathcal{F}_3^{2\gamma}}{G_M}\right), \quad (10)$$

$$\frac{P_l}{P_l^{\mathrm{Born}}} = 1-\frac{2\varepsilon}{1+\frac{\varepsilon}{\tau}\frac{G_E^2}{G_M^2}}\frac{1+\tau}{\tau}\frac{G_E}{G_M^3}\left(F_2\Re\mathcal{G}_M^{2\gamma}-G_M\Re\mathcal{F}_2^{2\gamma}\right) -\frac{2\varepsilon}{1+\frac{\varepsilon}{\tau}\frac{G_E^2}{G_M^2}}\left(\frac{\varepsilon}{1+\varepsilon}\left(1-\frac{G_E^2}{\tau G_M^2}\right)+\frac{G_E}{\tau G_M}\right) \times\frac{\nu}{M^2}\frac{\Re\mathcal{F}_3^{2\gamma}}{G_M}. \quad (11)$$

For further use, it will be convenient to introduce amplitudes $\mathcal{G}_1$, $\mathcal{G}_2$ defined as

$$\mathcal{G}_1^{2\gamma} = \mathcal{G}_M^{2\gamma} + \frac{\nu}{M^2}\mathcal{F}_3^{2\gamma}, \tag{12}$$

$$\mathcal{G}_2^{2\gamma} = \mathcal{G}_M^{2\gamma} - (1+\tau)\,\mathcal{F}_2^{2\gamma} + \frac{\nu}{M^2}\mathcal{F}_3^{2\gamma}. \tag{13}$$

In terms of these amplitudes, the TPE correction to the unpolarized cross section and the polarization transfer observables can be written as

$$\delta_{2\gamma} = \frac{2}{G_M^2 + \frac{\varepsilon}{\tau}G_E^2}\left\{G_M \Re\mathcal{G}_1^{2\gamma} + \frac{\varepsilon}{\tau}G_E\Re\mathcal{G}_2^{2\gamma} + G_M(\varepsilon-1)\frac{\nu}{M^2}\Re\mathcal{F}_3^{2\gamma}\right\}, \tag{14}$$

$$\frac{P_t}{P_l} = -\sqrt{\frac{2\varepsilon}{\tau(1+\varepsilon)}}\left(\frac{G_E}{G_M} + \frac{\Re\mathcal{G}_2^{2\gamma}}{G_M} - \frac{G_E}{G_M}\frac{\Re\mathcal{G}_1^{2\gamma}}{G_M} + \frac{1-\varepsilon}{1+\varepsilon}\frac{G_E}{G_M}\frac{\nu}{M^2}\frac{\Re\mathcal{F}_3^{2\gamma}}{G_M}\right), \tag{15}$$

$$\frac{P_l}{P_l^{\rm Born}} = 1 - \frac{2\varepsilon}{1+\frac{\varepsilon}{\tau}\frac{G_E^2}{G_M^2}}\left\{\frac{G_E}{\tau G_M}\frac{\Re\mathcal{G}_2^{2\gamma}}{G_M} - \frac{G_E^2}{\tau G_M^2}\frac{\Re\mathcal{G}_1^{2\gamma}}{G_M} + \left(\frac{\varepsilon}{1+\varepsilon} + \frac{1}{1+\varepsilon}\frac{G_E^2}{\tau G_M^2}\right)\frac{\nu}{M^2}\frac{\Re\mathcal{F}_3^{2\gamma}}{G_M}\right\}. \tag{16}$$

3 Dispersion relation formalism

In this work, we will calculate the TPE corrections to the invariant amplitudes $\mathcal{G}_M^{2\gamma}$, $\mathcal{F}_2^{2\gamma}$ and $\mathcal{F}_3^{2\gamma}$ in a dispersion relation (DR) formalism. For simplicity of notation, we will drop the subscript 2γ on the invariant amplitudes in all of the following of this paper, and understand that we already subtracted off the 1γ parts.

Assuming analyticity, one can write down DRs for the invariant amplitudes. As a consequence of Cauchy's theorem the real parts of the structure amplitudes can be obtained from the imaginary parts with the help of DRs expressed in the complex plane of the ν variable for fixed value of momentum transfer Q^2. The imaginary parts of the amplitudes which enter the DRs are related using unitarity to physical observables. The DRs require the amplitudes to have a sufficiently falling behavior at high energies to ensure convergence, otherwise a subtraction is required.

In this section, we will set up the details of the DR formalism for the TPE contribution to elastic e^-p scattering, and apply it to the case of a proton intermediate state.

3.1 Unitarity relation

The imaginary parts of the invariant amplitudes can be obtained with the help of the unitarity equation for the scattering matrix S (with $S = 1 + iT$)

$$S^+S = 1, \qquad T^+T = i(T^+ - T). \tag{17}$$

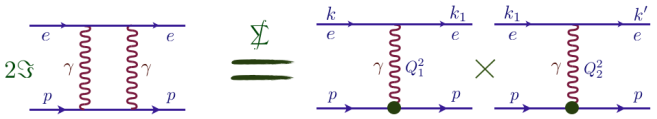

Fig. 2. Unitarity relations for the case of the elastic intermediate state contribution.

For the numerical estimates in this paper, we will consider the unitarity relations for the nucleon intermediate state contribution, which by definition only involves on-shell amplitudes in the 1γ-exchange approximation. The unitarity relation is represented in fig. 2.

In the c.m. frame, the electron energy is $k_0 = (s - M^2)/(2\sqrt{s})$. The electron initial ($k$), intermediate ($k_1$) and final ($k'$) momentums are given by

$$\begin{aligned} k &= k_0(1,0,0,1),\\ k_1 &= k_0(1,\sin\theta_1\cos\phi_1, \sin\theta_1\sin\phi_1, \cos\theta_1),\\ k' &= k_0(1,\sin\theta_{\rm cm},0,\cos\theta_{\rm cm}), \end{aligned} \tag{18}$$

with intermediate electron angles θ_1 and ϕ_1.

We also introduce the relative angle between the 3-momentum of intermediate and final electrons as $\hat{k}_1\cdot\hat{k}' \equiv \cos\theta_2$, with $\cos\theta_2 = \cos\theta_{\rm cm}\cos\theta_1 + \sin\theta_{\rm cm}\sin\theta_1\cos\phi_1$.

The imaginary parts of the 2γ-exchange helicity amplitudes are given by

$$\begin{aligned} \Im T_1 &= \frac{1}{64\pi^2}\frac{s-M^2}{s}\int\left\{T_1^{1\gamma}(Q_1^2)T_1^{1\gamma}(Q_2^2) + T_2^{1\gamma}(Q_1^2)T_2^{1\gamma}(Q_2^2)\cos(\tilde{\phi}')\right\}\mathrm{d}\Omega,\\ \Im T_3 &= \frac{1}{64\pi^2}\frac{s-M^2}{s}\int\left\{T_3^{1\gamma}(Q_1^2)T_3^{1\gamma}(Q_2^2)\cos(\phi-\phi') - T_2^{1\gamma}(Q_1^2)T_2^{1\gamma}(Q_2^2)\cos(\phi+\tilde{\phi})\right\}\mathrm{d}\Omega,\\ \Im T_2 &= \frac{1}{64\pi^2}\frac{s-M^2}{s}\int\left\{T_2^{1\gamma}(Q_1^2)T_3^{1\gamma}(Q_2^2)\cos(\phi') + T_1^{1\gamma}(Q_1^2)T_2^{1\gamma}(Q_2^2)\cos(\tilde{\phi})\right\}\mathrm{d}\Omega, \end{aligned} \tag{19}$$

where the phases ϕ, ϕ', $\tilde{\phi}$, $\tilde{\phi}'$ are defined in eq. (A.1) of appendix A. The momentum transfers Q_1^2 and Q_2^2 correspond with the scattering from initial to intermediate state and with the scattering from intermediate to final state respectively. The 1γ-exchange amplitudes, which were defined in eq. (19) by explicitly taking out all kinematical phases, can be obtained from eq. (3) after substitution of the structure amplitudes by the corresponding FFs: $\mathcal{G}_M \to G_M$, $\mathcal{F}_2 \to F_2$, $\mathcal{F}_3 \to 0$ and are given by

$$\begin{aligned} T_1^{1\gamma} &= 2\frac{e^2}{Q^2}\left\{\frac{su-M^4}{s-M^2}(F_2 - G_M) + Q^2 G_M\right\},\\ T_2^{1\gamma} &= -\frac{e^2}{Q^2}\frac{\sqrt{Q^2(M^4-su)}}{M}\left\{F_2 + 2\frac{M^2}{s-M^2}(F_2 - G_M)\right\},\\ T_3^{1\gamma} &= 2\frac{e^2}{Q^2}\frac{su-M^4}{s-M^2}(F_2 - G_M). \end{aligned} \tag{20}$$

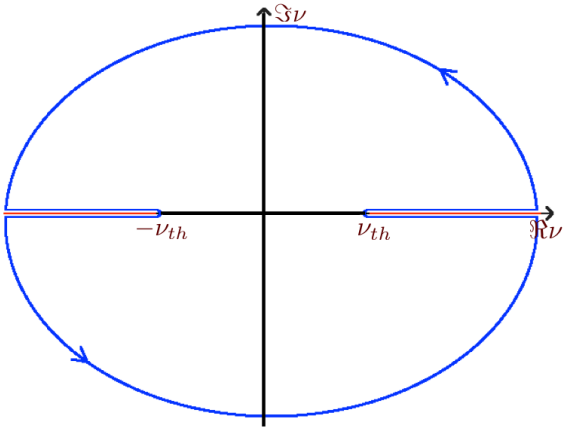

Fig. 3. Complex plane of the ν variable.

In the case of the forward scattering $\sin(\theta_{\rm cm}) = 0$, $\cos(\theta_{\rm cm}) = 1$, the unitarity relations lead to the optical theorem for amplitudes without helicity flip of the proton. The proton helicity-flip amplitude T_2 vanishes in this limit.

3.2 Dispersion relations

To discuss DRs for the invariant amplitudes describing the elastic e^-p scattering it is convenient to use amplitudes which have a definite behavior under $s \leftrightarrow u$ crossing symmetry. In terms of the crossing symmetry variable $\nu = (s-u)/4$, one can verify that the TPE invariant amplitudes have following crossing symmetry properties:

$$\begin{aligned} &\mathcal{G}_1(-\nu, Q^2) = -\mathcal{G}_1(\nu, Q^2), \quad \mathcal{G}_2(-\nu, Q^2) = -\mathcal{G}_2(\nu, Q^2), \\ &\mathcal{G}_M(-\nu, Q^2) = -\mathcal{G}_M(\nu, Q^2), \quad \mathcal{F}_2(-\nu, Q^2) = -\mathcal{F}_2(\nu, Q^2), \\ &\mathcal{F}_3(-\nu, Q^2) = \mathcal{F}_3(\nu, Q^2). \end{aligned} \tag{21}$$

The general form of fixed-Q^2 DR for the function with definite crossing symmetry properties can be obtained from the complex plane shown in fig. 3 and is given by

$$\Re\mathcal{G}(\nu, Q^2) = \frac{1}{\pi}\left(\int_{\nu_{th}}^{\infty} \frac{\Im\mathcal{G}(\nu'+i0, Q^2)}{\nu'-\nu}\,{\rm d}\nu' - \int_{-\infty}^{-\nu_{th}} \frac{\Im\mathcal{G}(\nu'-i0, Q^2)}{\nu'-\nu}\,{\rm d}\nu'\right). \tag{22}$$

The dispersive integral starts from the threshold ν_{th} corresponding with the cut. The threshold corresponding with the elastic cut due to the nucleon intermediate state is located at $s = M^2$ or $\nu_{th} = \nu_B = -Q^2/4$, so there is an integration region with intersection of s- and u-channel cuts. The threshold corresponding with the inelastic cut due to the pion-nucleon intermediate states is given by $s = (M + m_\pi)^2$ or $\nu_{th} = m_\pi(m_\pi + 2M)/2 - Q^2/4$.

The amplitudes which are odd in ν, $\mathcal{G}^{\rm odd}$, satisfy

$$\Re\mathcal{G}^{\rm odd}(\nu, Q^2) = \frac{2}{\pi}\nu\int_{\nu_{th}}^{\infty} \frac{\Im\mathcal{G}^{\rm odd}(\nu'+i0, Q^2)}{\nu'^2-\nu^2}\,{\rm d}\nu'. \tag{23}$$

Table 1. The values of the powers x_1 and x_2 in the HE fit of the different structure amplitudes according to the form $\mathcal{G}(\nu) \simeq (c_1\nu^{x_1} + c_2\nu^{x_2}\ln\nu)$, for the box diagram model with point-like F_1F_1 vertex structure.

	$\Im\mathcal{G}_M$	$\Im\mathcal{F}_2$	$\Im\mathcal{F}_3$	$\Im\mathcal{G}_1$	$\Im\mathcal{G}_2$
x_1	0	−2	−1	−1	−1
x_2	0	−2	−1	−1	−1
	$\Re\mathcal{G}_M$	$\Re\mathcal{F}_2$	$\Re\mathcal{F}_3$	$\Re\mathcal{G}_1$	$\Re\mathcal{G}_2$
x_1	0	−1	−1	−1	−1
x_2	0	−1	−1	−1	−1

Table 2. Same as table 1, but for the box diagram model with point-like F_1F_2 vertex structure.

	$\Im\mathcal{G}_M$	$\Im\mathcal{F}_2$	$\Im\mathcal{F}_3$	$\Im\mathcal{G}_1$	$\Im\mathcal{G}_2$
x_1	0	−1	−1	−1	−1
x_2	0	−1	−1	−1	−1
	$\Re\mathcal{G}_M$	$\Re\mathcal{F}_2$	$\Re\mathcal{F}_3$	$\Re\mathcal{G}_1$	$\Re\mathcal{G}_2$
x_1	0	−1	−1	−1	−1
x_2	0	−1	−1	−1	−1

Table 3. Same as table 1, but for the box diagram model with point-like F_2F_2 vertex structure.

	$\Im\mathcal{G}_M$	$\Im\mathcal{F}_2$	$\Im\mathcal{F}_3$	$\Im\mathcal{G}_1$	$\Im\mathcal{G}_2$
x_1	0	−1	−1	0	0
x_2	0	−1	−1	0	0
	$\Re\mathcal{G}_M$	$\Re\mathcal{F}_2$	$\Re\mathcal{F}_3$	$\Re\mathcal{G}_1$	$\Re\mathcal{G}_2$
x_1	1	−1	0	0	0
x_2	0	−1	−1	−1	−1

The amplitudes which are even in ν, $\mathcal{G}^{\rm even}$, satisfy

$$\Re\mathcal{G}^{\rm even}(\nu, Q^2) = \frac{2}{\pi}\int_{\nu_{th}}^{\infty} \nu'\frac{\Im\mathcal{G}^{\rm even}(\nu'+i0, Q^2)}{\nu'^2-\nu^2}\,{\rm d}\nu'. \tag{24}$$

Unsubtracted DRs as given by eqs. (23) and (24) can only be written down for functions with appropriate high-energy (HE) behavior. We will next discuss the HE behavior of the structure amplitudes for the case of the box diagram calculation with nucleon intermediate state, which will be explained in detail in sect. 4.

For the discussions of the HE behavior in the box diagram model with nucleon intermediate state, we consider the virtual photon-proton-proton vertices as point couplings. Furthemore, we consider three contributions, whether both vertices correspond with vector couplings (referred to as F_1F_1 structure), both vertices correspond with tensor couplings (F_2F_2 structure), or whether one vertex corresponds with a vector and the second vertex with a tensor coupling (F_1F_2 structure).

In general, the HE behavior ($\nu \gg Q^2, M^2$) of the amplitudes can be parametrized as $\mathcal{G}(\nu) \simeq (c_1\nu^{x_1} + c_2\nu^{x_2}\ln\nu)$, where the parameters can be extracted from a fit to the calculation. In tables 1–3, we show the extracted

values of the powers x_1, x_2 for the different structure amplitudes and for the different cases of virtual photon-proton-proton vertices.

For the case of F_1F_1 and F_1F_2 vertex structures, one notices that the behaviors of all amplitudes are sufficient to ensure unsubtracted DRs. For the case of two magnetic vertices (F_2F_2 structure), we notice that the $\mathcal{F}_2$, $\mathcal{G}_1$, $\mathcal{G}_2$ amplitudes are sufficiently convergent to satisfy an unsubtracted DR. However, after UV regularization the amplitude $\mathcal{G}_M$ ($\mathcal{F}_3$) has a real part which is behaving as ν (ν^0) respectively, which in both cases leads to a constant contribution due to the contour at infinity in Cauchy's integral formula. This constant term cannot be reconstructed from the imaginary part of the amplitude. To avoid such unknown contribution, we will use in our following calculations instead of the amplitudes $\mathcal{G}_M$ and $\mathcal{F}_2$, which are odd in ν, the amplitudes $\mathcal{G}_1$ and $\mathcal{G}_2$, defined in eqs. (12) and (13). As is clear from the tables 1–3, the amplitudes $\mathcal{G}_1$ and $\mathcal{G}_2$ both satisfy unsubtracted DRs.

For the amplitude $\mathcal{F}_3$, which is even in ν, and for which an UV regularization has to be performed in the box diagram model when using point-like couplings, we will in the following compare the unsubtracted DR with a once-subtracted DR, with subtraction at a low energy point ν_0, of the form

$$\Re\mathcal{G}^{\rm even}(\nu,Q^2)-\Re\mathcal{G}^{\rm even}(\nu_0,Q^2)= \frac{2\left(\nu^2-\nu_0^2\right)}{\pi}\int_{\nu_{th}}^{\infty}\frac{\nu'\Im\mathcal{G}^{\rm even}(\nu'+i0,Q^2)}{\left(\nu'^2-\nu^2\right)\left(\nu'^2-\nu_0^2\right)}\,{\rm d}\nu'. \tag{25}$$

3.3 Analytical continuation into the unphysical region

To evaluate the dispersive integral at a fixed value of momentum transfer $t=-Q^2$ we have to know the imaginary part of the structure amplitude from the threshold in energy onwards. The imaginary part evaluated from the unitarity relations by performing a phase space integration over physical angles covers only the "physical" region of integration. The structure amplitudes also have an imaginary part outside the physical region as long as one is above the threshold energy. Accounting for only the contribution of the physical region to the structure amplitudes is in contradiction with the results obtained from the direct box graph evaluation for the electron-muon scattering [50]. Starting from the imaginary part of the structure amplitude in the physical region, we will now discuss how to continue it analytically into the unphysical region. To illustrate the physical and unphysical regions, we show in fig. 4 the Mandelstam plot for elastic electron-proton scattering in the limit of massless electrons.

The threshold of the physical region is defined by the hyperbola

$$\nu=\nu_{ph}\equiv\frac{\sqrt{Q^2(Q^2+4M^2)}}{4}. \tag{26}$$

Therefore, the evaluation of the dispersive integral for the elastic intermediate state at $t=-Q^2<0$ always requires information from the unphysical region. Note that

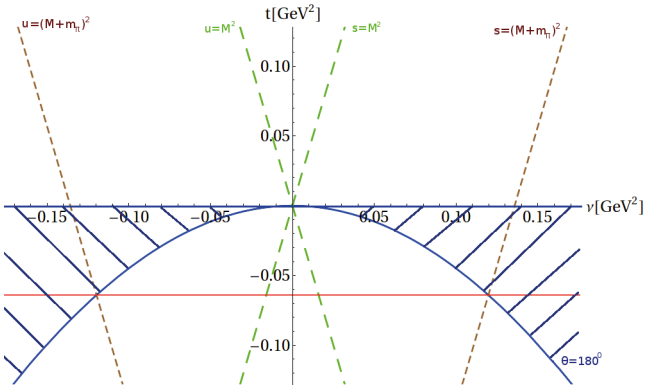

Fig. 4. Physical and unphysical regions of the kinematical variables ν and $t=-Q^2$ (Mandelstam plot). The hatched blue region corresponds to the physical region, the long-dashed green lines give the elastic threshold positions, the short-dashed brown lines give the inelastic threshold positions. The horizontal red curve indicates the line at fixed negative t along which the dispersive integrals are evaluated.

for $-t=Q^2<4m_\pi^2(1+\frac{m_\pi}{2M})^2/(1+\frac{m_\pi}{M})^2\simeq 0.064\,{\rm GeV}^2$ (indicated by the red horizontal line in fig. 4) an analytical continuation into the unphysical region is only required for the evaluation of the cut in the box diagram due to the nucleon intermediate states. For Q^2 larger than this value, also the evaluation of the cut due to the πN inelastic intermediate states requires an analytical continuation into the unphysical region.

We next discuss the integration region entering the unitarity relations for the case of the nucleon intermediate state contribution. The momentum transfers for the 1γ-exchange processes entering the r.h.s. of the unitarity relations eq. (19) are given by

$$Q_1^2=\frac{(s-M^2)^2}{2s}\left(1-\cos\theta_1\right),\qquad Q_2^2=\frac{(s-M^2)^2}{2s}\left(1-\cos\theta_2\right). \tag{27}$$

The indices 1, 2 correspond to scattering from initial to intermediate state and from intermediate to final state. The momentum transfer Q^2 obtains its maximal value for backward scattering $\theta=180^\circ$. If Q_i^2 is maximal (*i.e.*, $\theta_i=180^\circ$), then Q_2^2 can be evaluated as

$$Q_1^2=Q_{\rm max}^2=\frac{(s-M^2)^2}{s},\qquad Q_2^2=\frac{1}{s}\left(\left(s-M^2\right)^2-sQ^2\right). \tag{28}$$

The phase space integration in eq. (19) maps out an ellipse in the Q_1^2, Q_2^2 plane, where the position of the major axis depends on the elastic scattering angle (or Q^2). The centre of the ellipse is located at $Q_1^2=Q_2^2=Q_{\rm max}^2/2\equiv Q_c^2$. For forward and backward scattering, the ellipse reduces to a line: $Q_1^2=Q_2^2$ for $\theta_{\rm cm}=0^0$, and $Q_2^2=Q_{\rm max}^2-Q_1^2$ for $\theta_{\rm cm}=180^\circ$. In fig. 5, we show the physical integration regions for different elastic scattering kinematics which we

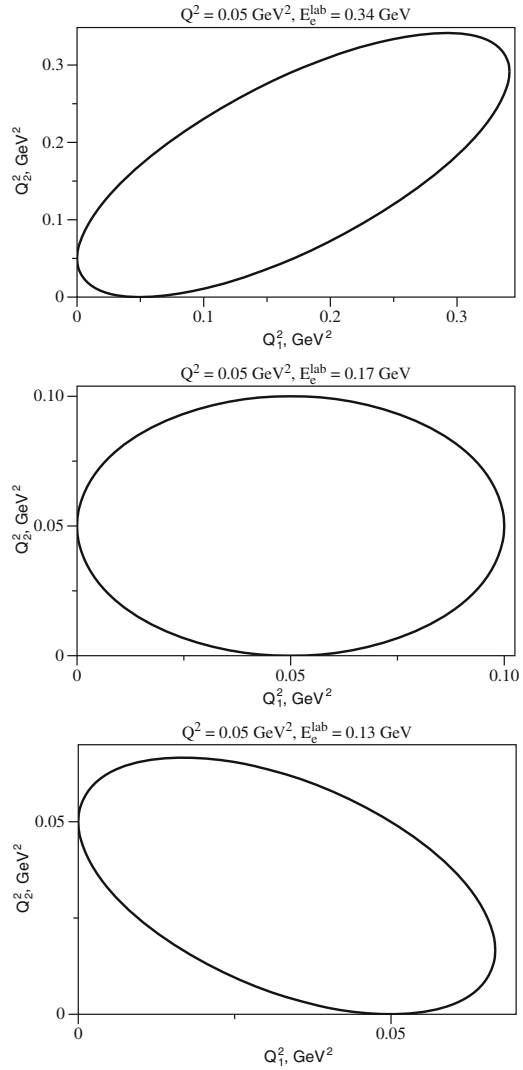

Fig. 5. The phase space integration regions entering the unitarity relations for the case of a nucleon intermediate state.

will consider in this work (the electron energy in the lab frame $E_e^{\rm lab}$, corresponding with a fixed target, is related to the s variable by $s = M^2 + 2ME_e^{\rm lab}$).

We will now demonstrate the procedure of analytical continuation on the example of the integral which corresponds with one denominator (originating from one of both photon propagators) on the r.h.s. of the unitarity relations eq. (19). We introduce a small photon mass μ to regulate IR singularities. The phase space integration entering the unitarity relations can be expressed in terms of elliptic coordinates α and ϕ (see appendix B) as

$$\int \frac{g(Q_1^2, Q_2^2)\,\mathrm{d}\Omega}{Q_{1,2}^2 + \mu^2} \sim \int_0^1 \mathrm{d}\alpha \int_0^{2\pi} \mathrm{d}\phi \times \frac{g\left(Q_c^2(a + b\cos\phi - c\sin\phi), Q_c^2(a + b\cos\phi + c\sin\phi)\right)}{a + b\cos\phi \mp c\sin\phi}, \tag{29}$$

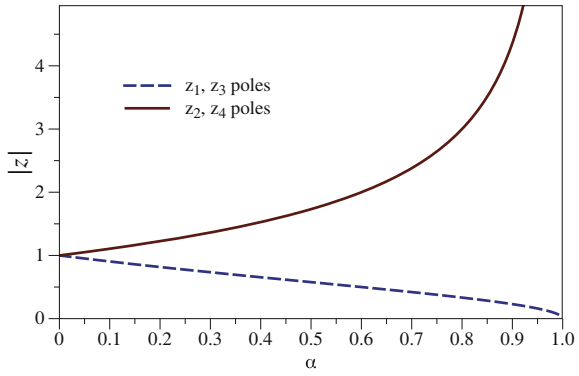

Fig. 6. The moduli of the pole positions in the physical region entering the angular integral in eq. (30) for $E_e^{\rm lab} = 0.3\,\mathrm{GeV}$, $\mu = 10^{-6}\,\mathrm{GeV}$. Note that these moduli do not depend on the momentum transfer Q^2. The poles z_1 and z_3 are inside the unit circle of integration ($|z| = 1$) for all values of α.

with

$$a = 1 + \frac{2s\mu^2}{(s - M^2)^2},$$

$$b = \sqrt{1 - \alpha^2}\sqrt{1 - \frac{sQ^2}{(s - M^2)^2}},$$

$$c = \sqrt{1 - \alpha^2}\sqrt{\frac{sQ^2}{(s - M^2)^2}}.$$

The angular integration can be performed on a unit circle in a complex plane with $z = e^{i\phi}$

$$\int_0^{2\pi} \mathrm{d}\phi \frac{g(Q_1^2, Q_2^2)}{a + b\cos\phi - c\sin\phi} = -i\oint \frac{g(Q_1^2, Q_2^2)}{b + ic}\frac{2\,\mathrm{d}z}{(z - z_1)(z - z_2)},$$

$$\int_0^{2\pi} \mathrm{d}\phi \frac{g(Q_1^2, Q_2^2)}{a + b\cos\phi + c\sin\phi} = -i\oint \frac{g(Q_1^2, Q_2^2)}{b - ic}\frac{2\,\mathrm{d}z}{(z - z_3)(z - z_4)}, \tag{30}$$

with poles position given by

$$z_{1,2} = \frac{1}{b + ic}\left(-a \pm \sqrt{a^2 - (1 - \alpha^2)}\right), \tag{31}$$

$$z_{3,4} = \frac{1}{b - ic}\left(-a \pm \sqrt{a^2 - (1 - \alpha^2)}\right). \tag{32}$$

In the physical region $(s - M^2)^2 > sQ^2$, the integral is given by the residues of the poles z_1, z_3 ("+" sign in eqs. (31) and (32)), see fig. 6.

In the unphysical region $(s - M^2)^2 < sQ^2$, the positions of the poles change with respect to the unit circle (fig. 7), so the integral has a discontinuity at the transition point. To avoid the discontinuities, we define an analytical continuation by deforming the integration contour so

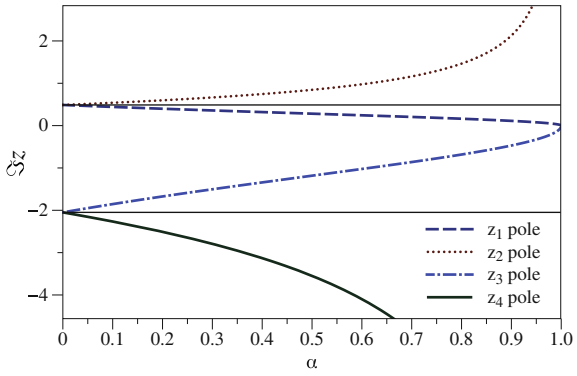

Fig. 7. Imaginary part of the poles in the unphysical region entering the angular integral in eq. (30) for $E_e^{\rm lab} = 0.3\,\text{GeV}$, $\mu = 10^{-6}\,\text{GeV}$, $Q^2 = 0.35\,\text{GeV}^2$ (for which $b_0 = 0.78$ and $c_0 = 1.27$). The poles lie on the imaginary axis in the unphysical region. The pole z_3 is outside the unit circle for the values $\alpha < \alpha_0 = 0.61$. The intersections of the new contour of integration with the imaginary axis are shown by the horizontal solid lines, corresponding with values $c_0 - b_0 \simeq 0.49$ (upper line) and $-c_0 - b_0 \simeq 2.05$ (lower line), respectively.

as to include the poles z_1 and z_3. The integration can be done on the circle of the radius c_0 and the centre $-ib_0$ as

$$\int_0^{2\pi} f(e^{i\phi})\mathrm{d}\phi = \oint_{|z|=1} -if(z)\frac{\mathrm{d}z}{z} \to \oint_{z=c_0 e^{i\phi}-ib_0} -if(z)\frac{\mathrm{d}z}{z}, \tag{33}$$

with

$$c_0 = \sqrt{sQ^2/(s-M^2)^2}, \qquad b_0 = \sqrt{-1+sQ^2/(s-M^2)^2}.$$

For the value $\alpha = 0$, when the expression in brackets of eqs. (31) and (32) approaches its minimum, the positions of the poles of interest (for small photon mass parameter $\mu \to 0$) are given by

$$\begin{aligned} z_1 &= \frac{i}{b_0+c_0}\left(1-\frac{2\mu\sqrt{s}}{s-M^2}\right) = i(c_0-b_0)\left(1-\frac{2\mu\sqrt{s}}{s-M^2}\right), \\ z_3 &= \frac{i}{b_0-c_0}\left(1-\frac{2\mu\sqrt{s}}{s-M^2}\right) = -i(c_0+b_0)\left(1-\frac{2\mu\sqrt{s}}{s-M^2}\right). \end{aligned} \tag{34}$$

These poles lie inside the deformed contour of integration which intersects the imaginary axis at $\Im z = c_0 - b_0$ and $\Im z = -c_0 - b_0$ respectively. We show in fig. 8 that with the growth of photon mass parameter μ the poles move further away from the boundary of the integration region and therefore lie inside the new contour of integration.

The deformed contour includes poles from both photon propagators, consequently the procedure of analytical continuation works also for two photon propagators in the unitarity relations eq. (19). Therefore, through analytical continuation, the unitarity relations are able to reproduce the imaginary part of the structure amplitudes in the unphysical region also. As a cross-check of our procedure, we show the imaginary part $\mathcal{G}_M$ for the case of electron-muon scattering in fig. 9, as calculated using the analytically

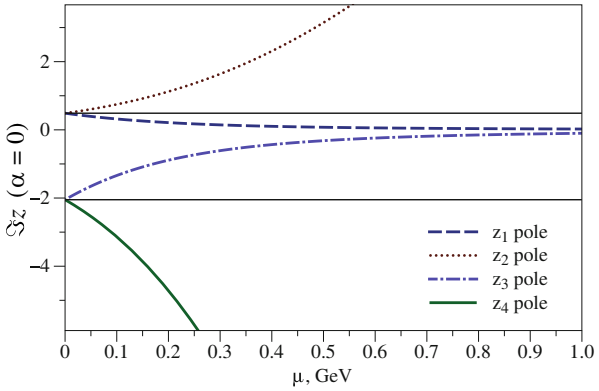

Fig. 8. Same as fig. 7 for $\alpha = 0$ as a function of μ.

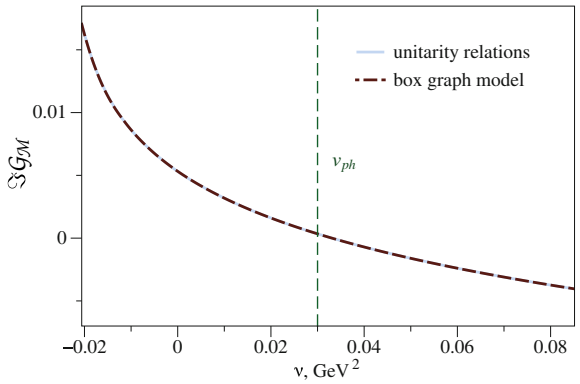

Fig. 9. Comparison between two evaluations of the imaginary part of the structure amplitude $\mathcal{G}_M$ for $e^-\mu^-$ scattering for $Q^2 = 0.1\,\text{GeV}^2$ corresponding with $\nu_{ph} = 0.03\,\text{GeV}^2$. Dash-dotted curve: box graph evaluation; solid curve (coinciding): evaluation based on the unitarity relations. The region $\nu > \nu_{ph}$ ($\nu < \nu_{ph}$) corresponds with the physical (unphysical) region, respectively.

continued phase space integral, and compare it with the direct loop graph evaluation as explained in sect. 4 [50]. We find a perfect agreement between both calculations, justifying our analytical continuation procedure for the calculation based on unitarity relations.

A more realistic description of the proton is obtained by including electromagnetic FFs of the dipole form. This induces additional poles for the time-like region $Q_i^2 < 0$ in the unitarity relations eq. (19)

$$G_M \sim \frac{1}{(Q_i^2+\Lambda^2)^2}, \qquad F_2 \sim \frac{1}{(Q_i^2+4M^2)(Q_i^2+\Lambda^2)^2}. \tag{35}$$

These poles arise from the dipole mass parameter Λ ($Q_i^2 + \Lambda^2 = 0$) and from the "kinematic" pole ($Q_i^2 + 4M^2 = 0$). These poles can be treated in a similar way as the poles in eqs. (31) and (32) through the replacement $\mu \to \Lambda$ or $\mu \to 2M$. These poles lie on the same line in the complex z plane as the z_1, z_2, z_3, z_4 poles. As soon as $\Lambda > \mu$, $2M > \mu$, the new poles satisfy $|z_1'| < |z_1|$, $|z_3'| < |z_3|$, $|z_2'| > |z_2|$, $|z_4'| > |z_4|$. From fig. 8, where the μ dependence of the pole positions in the unphysical region is shown, we see that our procedure of analytical continuation does

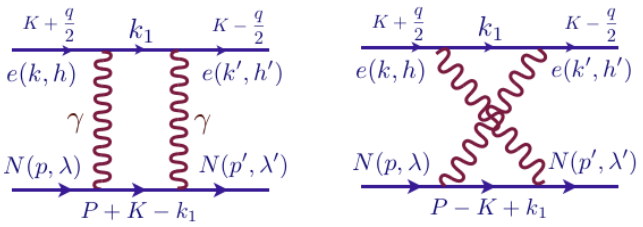

Fig. 10. Direct and crossed TPE diagrams in $e^- p$ elastic scattering.

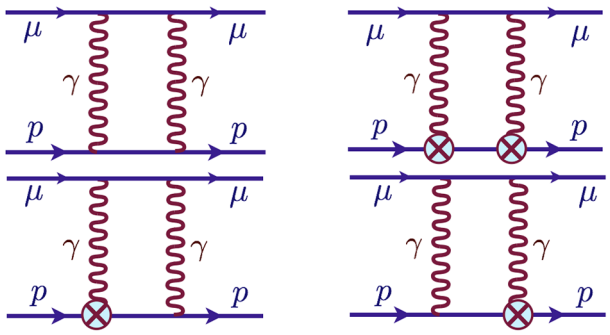

Fig. 11. The different contributions to the proton box diagram, depending on the different virtual photon-proton-proton vertices. The vertex with (without) the cross denotes the contribution proportional to the F_2 (F_1) FF. The different diagrams show the F_1F_1 (upper left panel), F_2F_2 (upper right panel) and F_1F_2 (lower panels) vertex structures.

not change the position of the new poles with respect to the deformed integration contour after the transition to the unphysical region. We can therefore conclude that the outlined procedure of analytical continuation is also valid for the calculation with proton FFs.

4 Box diagram model calculation

In this section, we will present the model which will be used in the following to check the applicability of DRs for the TPE contribution to elastic electron-proton scattering. For this purpose, we will evaluate the box graph elastic contribution (corresponding with a nucleon intermediate state) to the structure amplitudes and compare it with the evaluation of the amplitudes using the DR formalism. In our calculation of the box diagram contribution, we will assume an on-shell form of the virtual photon-proton-proton vertex.

4.1 Loop diagram evaluation

We will consider the TPE direct and crossed box graph contributions to the structure amplitudes, as shown in fig. 10. The helicity amplitudes corresponding with the TPE direct and crossed graphs can be expressed as

$$\begin{aligned}
T_{\rm direct} = -ie^4 \int \frac{\mathrm{d}^4 k_1}{(2\pi)^4} \bar{u}(k',h')\gamma^\mu(\hat{k_1}+m)\gamma^\nu u(k,h) \\
\times \bar{N}(p',\lambda')\Gamma_\mu(\hat{P}+\hat{K}-\hat{k}_1+M)\Gamma_\nu N(p,\lambda) \\
\times \frac{1}{(k_1-P-K)^2-M^2}\frac{1}{k_1^2-m^2} \\
\times \frac{1}{(k_1-K-\frac{q}{2})^2-\mu^2}\frac{1}{(k_1-K+\frac{q}{2})^2-\mu^2}\,, \\
T_{\rm crossed} = -ie^4 \int \frac{\mathrm{d}^4 k_1}{(2\pi)^4} \bar{u}(k',h')\gamma^\mu(\hat{k_1}+m)\gamma^\nu u(k,h) \\
\times \bar{N}(p',\lambda')\Gamma_\nu(\hat{P}-\hat{K}+\hat{k}_1+M)\Gamma_\mu N(p,\lambda) \\
\times \frac{1}{(k_1+P-K)^2-M^2}\frac{1}{k_1^2-m^2} \\
\times \frac{1}{(k_1-K-\frac{q}{2})^2-\mu^2}\frac{1}{(k_1-K+\frac{q}{2})^2-\mu^2}\,,
\end{aligned} \tag{36}$$

where Γ^μ denotes the virtual photon-proton-proton vertex, m denotes the lepton mass which will be neglected in the following calculations, and where the notation $\hat{a} \equiv \gamma^\mu a_\mu$ was used. The structure amplitudes entering eq. (9) can be expressed as combination of helicity amplitudes with the help of eq. (4).

We perform the box diagram calculation with the assumption of an on-shell form of the virtual photon-proton-proton vertex

$$\Gamma^\mu(Q^2) = \gamma^\mu F_1(Q^2) + \frac{i\sigma^{\mu\nu}q_\nu}{2M}F_2(Q^2), \tag{37}$$

for two models. In the first model the proton is treated as a point particle with charge and anomalous magnetic moment, *i.e.*, the Dirac and Pauli FFs in eq. (37) have the following form:

$$F_1 = 1, \qquad F_2 = \kappa. \tag{38}$$

The second model is more realistic and it based on the dipole form for the proton electromagnetic FFs

$$\begin{aligned}
G_M = F_1 + F_2 = \frac{\kappa+1}{(1+\frac{Q^2}{\Lambda^2})^2}\,, \\
G_E = F_1 - \tau F_2 = \frac{1}{(1+\frac{Q^2}{\Lambda^2})^2}\,,
\end{aligned} \tag{39}$$

with $\kappa = 1.793$ and $\Lambda^2 = 0.71\,\mathrm{GeV}^2$.

Due to the photon momentum in the numerator of the term proportional to the FF F_2, the high-energy behavior of the amplitudes will be different depending on whether F_1 or F_2 enters the vertex. We denote the contribution with two vector coupling vertices by F_1F_1, two tensor couplings by F_2F_2, and the contributions from the mixed case by F_1F_2, see fig. 11. We have discussed the HE behavior of the structure amplitudes in case of point-like couplings in tables 1–3. The inclusion of FFs of the dipole form leads to an UV finite results for the structure amplitudes.

We use LOOPTOOLS [51, 52] to evaluate the four-point integrals and derivatives of them, as well as to provide a numerical evaluation of the structure amplitudes. The TPE amplitude $\mathcal{G}_M$ in the case of scattering of two

point charges (*i.e.*, F_1F_1 contribution with $F_1 = 1$) has the IR divergent term

$$\mathcal{G}_M^{\mathrm{IR,\,point}} = \frac{\alpha_{\mathrm{EM}}}{\pi} \ln\left(\frac{Q^2}{\mu^2}\right) \left\{ \ln\left(\frac{|u-M^2|}{s-M^2}\right) + i\pi \right\}, \tag{40}$$

with $\alpha_{\mathrm{EM}} \equiv e^2/4\pi \simeq 1/137$. When including FFs, the F_1F_1 vertex structure gives rise to an IR divergence in the amplitude $\mathcal{G}_M$ which is given by $\mathcal{G}_M^{\mathrm{IR},F_1F_1} = F_1(Q^2)\,\mathcal{G}_M^{\mathrm{IR,point}}$, whereas the F_1F_1 contributions to the amplitudes $\mathcal{F}_2$ and $\mathcal{F}_3$ are IR finite. The F_1F_2 vertex structure gives rise to IR divergences in the amplitude $\mathcal{G}_M$ as well as $\mathcal{F}_2$ which are given by $\mathcal{G}_M^{\mathrm{IR},F_1F_2} = \mathcal{F}_2^{\mathrm{IR},F_1F_2} = F_2(Q^2)\,\mathcal{G}_M^{\mathrm{IR,point}}$, whereas the F_1F_2 contribution to the amplitude $\mathcal{F}_3$ is IR finite. Finally, the F_2F_2 vertex structure contribution to all these amplitudes is IR finite. When combining all IR divergent pieces, eq. (9) yields the IR divergent TPE correction

$$\delta_{2\gamma}^{\mathrm{IR}} = \frac{2\alpha_{\mathrm{EM}}}{\pi} \ln\left(\frac{Q^2}{\mu^2}\right) \ln\left(\frac{|u-M^2|}{s-M^2}\right). \tag{41}$$

When comparing with data, which are radiatively corrected, we subtract eq. (41) in the cross section formula of eq. (9). This is in agreement with the Maximon and Tjon (MaTj) prescription for the soft photon TPE contribution, *i.e.*, $\delta_{2\gamma,\,\mathrm{soft}}^{\mathrm{MaTj}} = \delta_{2\gamma}^{\mathrm{IR}}$, see eq. (3.39) of ref. [53]. Note that the P_t and P_l observables, eqs. (15) and (16), are free of IR divergencies.

4.2 Dispersive evaluation

We next discuss the evaluation of the box diagram contributions with nucleon intermediate states using DRs. We perform DR calculations separately for F_1F_1, F_1F_2 and F_2F_2 vertex structures (fig. 11) for both FF models described above in eqs. (38) and (39).

For the point-like model, we obtain analytical expressions for the imaginary part of the structure amplitudes. The imaginary parts of the structure amplitudes due to the F_1F_1 vertex structure are given by

$$\begin{aligned}
\Im\mathcal{G}_M &= \alpha_{\mathrm{EM}} \Bigg\{ \ln\left(\frac{Q^2}{\mu^2}\right) - \frac{s+M^2}{2s} \\
&\quad - \frac{2(s-M^2)^2 - sQ^2}{2\left((s-M^2)^2 - sQ^2\right)} \ln\left(\frac{sQ^2}{(s-M^2)^2}\right) \Bigg\}, \\
\Im\mathcal{F}_2 &= \frac{\alpha_{\mathrm{EM}} M^2 Q^2}{(s-M^2)^2 - sQ^2} \\
&\quad \times \left\{ 1 + \frac{(s-M^2)^2}{(s-M^2)^2 - sQ^2} \ln\left(\frac{sQ^2}{(s-M^2)^2}\right) \right\}, \\
\Im F_3 &= \frac{\alpha_{\mathrm{EM}} M^2 (s-M^2)}{(s-M^2)^2 - sQ^2} \Bigg\{ \frac{s+M^2}{s} \\
&\quad + \frac{(s-M^2)\left(2(s-M^2) - Q^2\right)}{(s-M^2)^2 - sQ^2} \ln\left(\frac{sQ^2}{(s-M^2)^2}\right) \Bigg\}.
\end{aligned} \tag{42}$$

The imaginary parts of the structure amplitudes due to the mixed F_1F_2 vertex structure are given by

$$\begin{aligned}
\Im\mathcal{G}_M &= \alpha_{\mathrm{EM}}\kappa \Bigg\{ \ln\left(\frac{Q^2}{\mu^2}\right) - \frac{M^2}{s} \\
&\quad + \frac{2(s-M^2)^2 - sQ^2}{2\left((s-M^2)^2 - sQ^2\right)} \ln\left(\frac{sQ^2}{(s-M^2)^2}\right) \Bigg\}, \\
\Im\mathcal{F}_2 &= \alpha_{\mathrm{EM}}\kappa \frac{M^2 Q^2}{(s-M^2)^2 - sQ^2} \\
&\quad \times \Bigg\{ 1 + \frac{(s-M^2)^2(s+2M^2) - s^2Q^2}{2M^2\left((s-M^2)^2 - sQ^2\right)} \\
&\quad \times \ln\left(\frac{sQ^2}{(s-M^2)^2}\right) \Bigg\} + \alpha_{\mathrm{EM}}\kappa \ln\left(\frac{Q^2}{\mu^2}\right), \\
\Im\mathcal{F}_3 &= \alpha_{\mathrm{EM}}\kappa \frac{M^2}{s\left((s-M^2)^2 - sQ^2\right)} \\
&\quad \times \Bigg\{ 2M^2(s-M^2) + sQ^2 \\
&\quad + \frac{s(s-M^2)^2\left(2(s-M^2) - Q^2\right)}{(s-M^2)^2 - sQ^2} \ln\left(\frac{sQ^2}{(s-M^2)^2}\right) \Bigg\}.
\end{aligned} \tag{43}$$

The imaginary parts of the structure amplitudes due to the F_2F_2 vertex structure are given by

$$\begin{aligned}
\Im\mathcal{G}_M &= \alpha_{\mathrm{EM}}\kappa^2 \frac{s-M^2}{2s} \Bigg\{ 1 + \frac{s^2Q^2}{4M^2\left((s-M^2)^2 - sQ^2\right)} \\
&\quad \times \ln\left(\frac{sQ^2}{(s-M^2)^2}\right) \Bigg\}, \\
\Im\mathcal{F}_2 &= -\frac{\alpha_{\mathrm{EM}}\kappa^2}{4} \frac{(s-M^2)Q^2}{(s-M^2)^2 - sQ^2} \\
&\quad \times \left\{ 1 + \frac{(s-M^2)^2}{(s-M^2)^2 - sQ^2} \ln\left(\frac{sQ^2}{(s-M^2)^2}\right) \right\}, \\
\Im\mathcal{F}_3 &= -\frac{\alpha_{\mathrm{EM}}\kappa^2}{4s\left((s-M^2)^2 - sQ^2\right)} \Bigg\{ 4M^2(s-M^2)^2 + sQ^2 \\
&\quad \times (s-3M^2) + \frac{\left(M^6 - 3M^2s^2 + 2s^3 - s^2Q^2\right) sQ^2}{(s-M^2)^2 - sQ^2} \\
&\quad \times \ln\left(\frac{sQ^2}{(s-M^2)^2}\right) \Bigg\}.
\end{aligned} \tag{44}$$

We checked that the numerical calculations of the imaginary part of the structure amplitudes are in agreement with predictions for the target normal spin asymmetry A_n [49] for the model with dipole form of electromagnetic FFs [54].

In sect. 5, we will compare the DR and the direct loop evaluations for the TPE contribution which results from the nucleon intermediate state.

4.3 Forward limit

Before presenting the numerical results for the TPE corrections at finite Q^2, we first discuss the forward limit. This limit is relevant to extract the proton charge radius from elastic scattering data. In the forward limit, corresponding with $Q^2 \to 0$ and $\varepsilon \to 1$, the TPE correction to the cross section is given by Coulomb photons from the F_1F_1 structure of virtual photon-proton-proton vertices. This result was first obtained for the electron-proton scattering in Dirac theory as the first order cross section correction by McKinley and Feshbach [46]. The so-called Feshbach correction to the cross section can be expressed analytically in terms of the laboratory scattering angle θ or the photon polarization parameter ε as

$$\delta_F = \pi\alpha_{\rm EM}\frac{\sin\frac{\theta}{2}-\sin^2\frac{\theta}{2}}{\cos^2\frac{\theta}{2}} \approx \pi\alpha_{\rm EM}\frac{\sqrt{1-\varepsilon}}{\sqrt{1-\varepsilon}+\sqrt{1+\varepsilon}}. \tag{45}$$

It is instructive to provide some analytical expressions for $\delta_{2\gamma}$ in the forward limit resulting from the F_1F_1 vertex contribution to the full box diagram calculation.

For the case of electron scattering off massless quarks (taken with unit charge) the TPE correction is given by [13]

$$\delta_{2\gamma} = \frac{\alpha_{\rm EM}}{\pi}\Bigg\{2\ln\left(\frac{Q^2}{\mu^2}\right)\ln\left(\frac{1-x}{1+x}\right) + \frac{x}{1+x^2}\left[\ln^2\left(\frac{1+x}{2x}\right)+\ln^2\left(\frac{1-x}{2x}\right)+\pi^2\right] - \frac{x}{1+x^2}\left[\ln\left(\frac{1-x^2}{4x^2}\right)-x\ln\left(\frac{1+x}{1-x}\right)\right]\Bigg\}, \tag{46}$$

with $x = \sqrt{1-\varepsilon}/\sqrt{1+\varepsilon}$ and $Q^2 = 4x\nu$. In the forward limit ($Q^2 \to 0$ and $\varepsilon \to 1$, at finite ν) we recover the Feshbach term and find large logarithmic correction terms in $(1-\varepsilon)$

$$\delta_{2\gamma} - \delta_{2\gamma}^{\rm IR} \longrightarrow \delta_F + \frac{\alpha_{\rm EM}}{\pi}\sqrt{\frac{1-\varepsilon}{2}}\ln\left(2(1-\varepsilon)\right) \times\left[\frac{1}{2}\ln\left(2(1-\varepsilon)\right)+1\right], \tag{47}$$

where the IR divergent TPE is given by the massless limit of eq. (41).

For the case of forward scattering off a massive point particle we also give the analytical form of the momentum transfer expansion of the F_1F_1 vertex contribution for the model with point particles. In the forward direction, only the amplitude $\mathcal{G}_2$ defined in eq. (13) survives since $\delta_{2\gamma} \to 2\Re\mathcal{G}_2$ in the forward limit. The F_1F_1 point vertex contribution to the imaginary part of $\mathcal{G}_2$ is obtained from eqs. (42) as

$$\Im\mathcal{G}_2^{F_1F_1} = \alpha_{\rm EM}\Bigg\{\ln\left(\frac{Q^2}{\mu^2}\right)+\frac{Q^2}{4s} + \frac{Q^2}{8}\frac{s}{\nu^2-\nu_{ph}^2}\ln\left(\frac{sQ^2}{(s-M^2)^2}\right)\Bigg\}, \tag{48}$$

with ν_{ph} as defined in eq. (26). Using the dispersion relation of eq. (23), we can express the real part of $\mathcal{G}_2$ in the forward limit (for $Q^2 \ll M^2$) in terms of Q^2 and the electron beam energy $E_e^{\rm lab}$ in the laboratory frame as

$$\Re\mathcal{G}_2^{F_1F_1} \longrightarrow \frac{\alpha_{\rm EM}}{\pi}\Bigg\{-\frac{Q^2}{2ME_e^{\rm lab}}\ln\left(\frac{Q^2}{\mu^2}\right)+\pi^2\frac{Q}{4E_e^{\rm lab}} + \frac{Q^2}{2ME_e^{\rm lab}}\ln\left(\frac{Q}{2E_e^{\rm lab}}\right)\left[\ln\left(\frac{Q}{2E_e^{\rm lab}}\right)+1\right] + {\rm O}\left(\frac{Q^2}{M^2}\right)\Bigg\}, \tag{49}$$

where we have dropped terms of order Q^2/M^2 which do not lead to any logarithmic enhancements in the near forward direction. Note that we can equivalently express eq. (49) through the variable ε using the kinematical relation $Q/E_e^{\rm lab} \simeq \sqrt{2(1-\varepsilon)}$, which holds in the forward direction. Equation (49) then allows to directly express $\delta_{2\gamma}$ in the forward direction as

$$\delta_{2\gamma} - \delta_{2\gamma}^{\rm IR} \longrightarrow \delta_F + \frac{\alpha_{\rm EM}}{\pi}\frac{Q^2}{ME_e^{\rm lab}}\ln\left(\frac{Q}{2E_e^{\rm lab}}\right) \times\left[\ln\left(\frac{Q}{2E_e^{\rm lab}}\right)+1\right]+{\rm O}\left(\frac{Q^2}{M^2}\right), \tag{50}$$

where the leading finite term (proportional to $Q/E_e^{\rm lab}$) is obtained as the Feshbach correction term δ_F, and where subleading logarithmic correction terms are also shown. We found that our forward limit result of eq. (50) agrees with an expression obtained some time ago [55][1].

We can similarly study the contributions of the F_1F_2 and F_2F_2 vertex structures to the amplitude $\mathcal{G}_2$ in the case of a point-like proton comparing their imaginary parts $\Im\mathcal{G}_2^{F_1F_2}$, and $\Im\mathcal{G}_2^{F_2F_2}$ with the expression for the F_1F_1 vertex structure $\Im\mathcal{G}_2^{F_1F_1}$ of eq. (48). The corresponding imaginary parts can be obtained from eqs. (43) and (44) as

$$\Im\mathcal{G}_2^{F_1F_2} = \alpha_{\rm EM}\frac{Q^2}{4M^2}\kappa\Bigg\{-\ln\left(\frac{Q^2}{\mu^2}\right)+\frac{2M^2}{s} - \frac{Q^2}{8}\frac{s}{\nu^2-\nu_{ph}^2}\ln\left(\frac{sQ^2}{(s-M^2)^2}\right)\Bigg\}, \tag{51}$$

$$\Im\mathcal{G}_2^{F_2F_2} = \alpha_{\rm EM}\frac{Q^2}{4M^2}\kappa^2\Bigg\{-\frac{s-2M^2}{2s}-\frac{Q^2}{16}\frac{s}{\nu^2-\nu_{ph}^2} \times\ln\left(\frac{sQ^2}{(s-M^2)^2}\right)-\frac{1}{2}\ln\left(\frac{sQ^2}{(s-M^2)^2}\right)\Bigg\}. \tag{52}$$

The Feshbach correction and the subleading logarithmic terms in the real part of the amplitude $\mathcal{G}_2^{F_1F_1}$, eq. (49),

[1] Note that in ref. [56], the finite logarithmic terms multiplying Q^2 were missed. Equation (50) shows that the elastic box contains terms proportional to $Q^2\ln(Q^2)$ and $Q^2\ln^2(Q^2)$, which lead to corrections in the near forward direction.

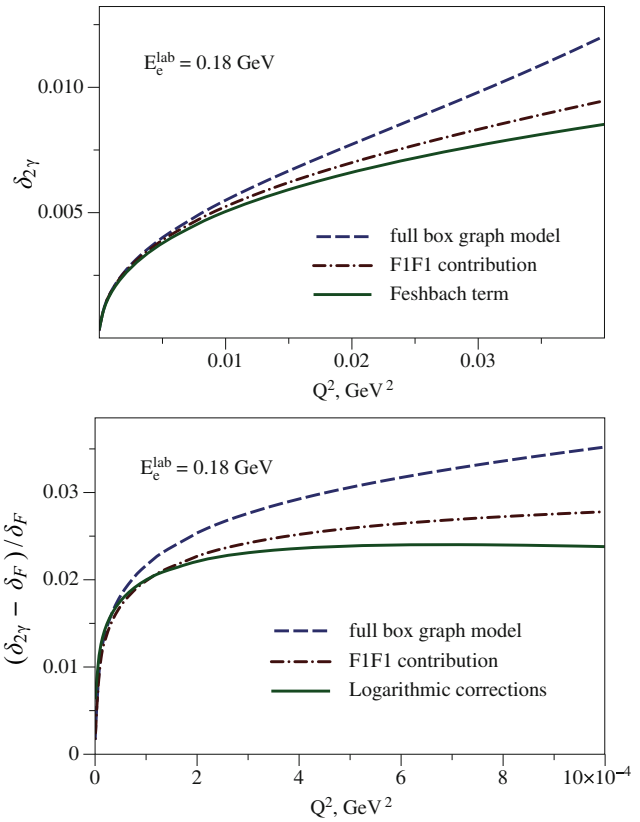

Fig. 12. The small Q^2-limit of the TPE correction in the model with a point-like proton for $E_e^{\rm lab} = 0.18\,{\rm GeV}$. For clarity, the contribution relative to the Feshbach term is shown on the right panels for the logarithmic correction term of eq. (50), for the F_1F_1 vertex contribution to the box diagram, and for the full box diagram calculation, also including the F_1F_2 and F_2F_2 contributions.

arise from the logarithmic term in eq. (48). Analogous terms are suppressed by the pre-factor Q^2/M^2 in the imaginary parts for the F_1F_2 and F_2F_2 vertex structures in comparison with the F_1F_1 vertex structure. The additional logarithmic term in eq. (52) also leads to corrections of higher order in Q/M in comparison with eq. (49). Besides the elastic contribution discussed here, ref. [55] also derived that in the forward limit, the $Q^2\ln(Q/2E_e^{\rm lab})$ term in eq. (50) obtains an additonal contribution due to inelastic states, which can be expressed through the total photo-production cross section on a nucleon.

In figs. 12 and 13 we compare the Feshbach correction with the full box diagram calculation of $\delta_{2\gamma}$ for point protons at low momentum transfers and at beam energies corresponding with experiments at MAMI and JLab. One sees that at small Q^2, the leading TPE contribution is given by the F_1F_1 vertex structure, and approaches the Feshbach term in the forward direction. We furthermore see that at small Q^2, the leading corrections to the Feshbach result are given by the logarithmic terms given in eq. (50).

In fig. 14, we compare the analogous results using the dipole model for the proton FFs.

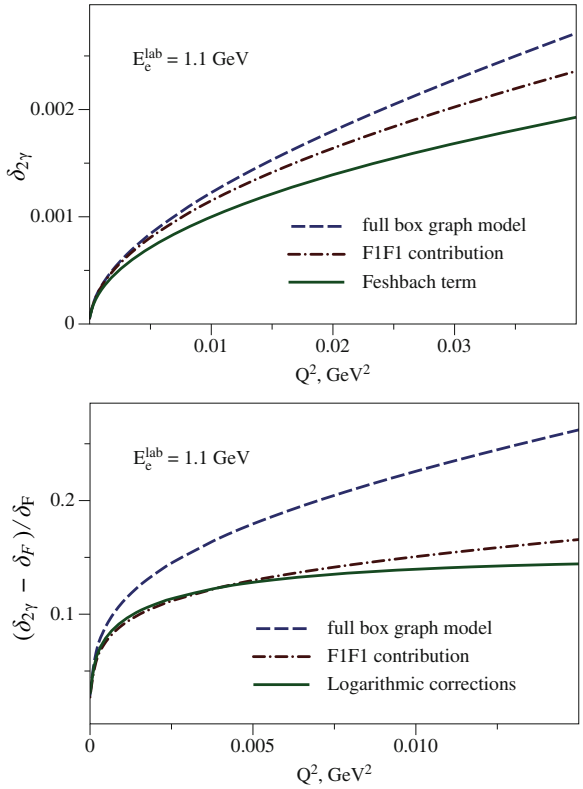

Fig. 13. Same as fig. 12, but for $E_e^{\rm lab} = 1.1\,{\rm GeV}$.

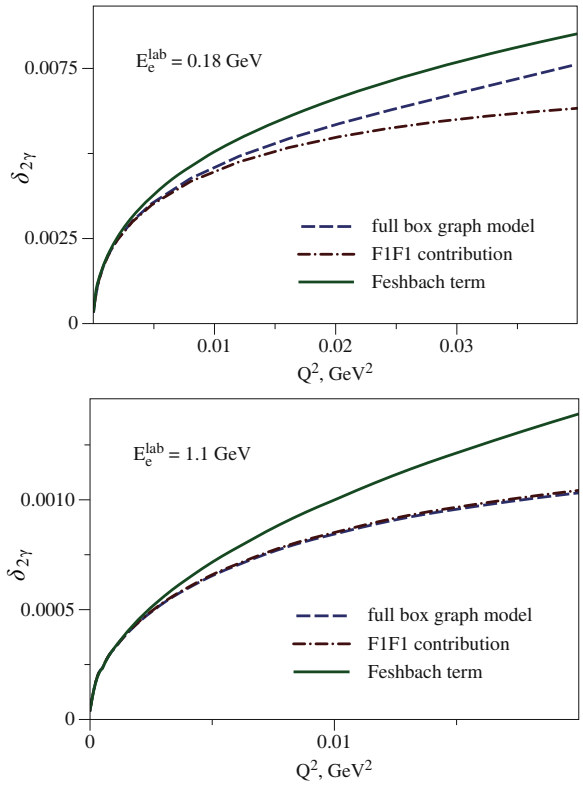

Fig. 14. The small Q^2-limit of the TPE correction in the model with dipole proton FFs for $E_e^{\rm lab} = 0.18\,{\rm GeV}$ (upper panel) and $E_e^{\rm lab} = 1.1\,{\rm GeV}$ (lower panel).

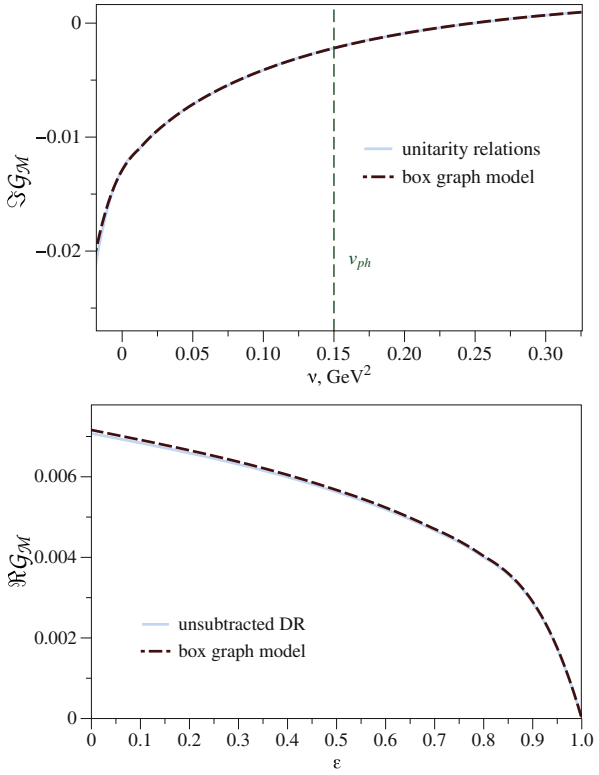

Fig. 15. Imaginary part (upper panel) and real part (lower panel) of the structure amplitude $\mathcal{G}_M$ for the F_1F_1 vertex structure with dipole FFs for $Q^2 = 0.1\,\mathrm{GeV}^2$. The vertical line in the left panel corresponds with the boundary between physical and unphysical regions, *i.e.*, $\nu_{ph} = 0.15\,\mathrm{GeV}^2$.

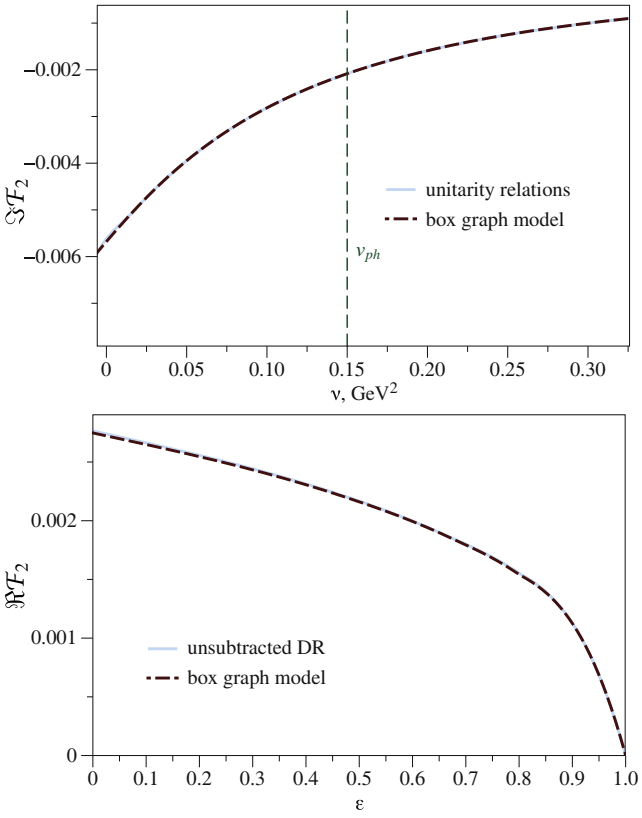

Fig. 16. Same as fig. 15, but for the structure amplitude $\mathcal{F}_2$.

5 Results and discussion

In this section, we firstly compare the model calculation of the elastic contribution to TPE amplitudes with the evaluation within the DR formalism. Subsequently, we discuss predictions for unpolarized and polarization transfer observables of elastic electron-proton scattering and compare with existing data.

The results for the real and imaginary parts of the amplitudes for the case of the F_1F_1 vertex structure in the model with dipole FFs are shown in figs. 15–17. We show the unitarity relations calculation of the imaginary parts of the structure amplitudes both in physical and unphysical regions. For the latter, we use the analytical continuation as outlined in sect. 3. For the imaginary parts, we see a perfect agreement between the unitarity relations calculations and the box graph evaluation both in physical and unphysical regions. We also checked that for the F_1F_2 and F_2F_2 vertex structures the imaginary parts of the structure amplitudes are in perfect agreement between the two approaches for all amplitudes and for both FF models. This is to be expected as the imaginary parts of the structure amplitudes correspond with an intermediate state in the box diagram which is on its mass shell. Therefore only on-shell information enters the imaginary parts.

For the real parts, we use the unsubtracted DRs at fixed Q^2. By comparing the DR results with the loop di-

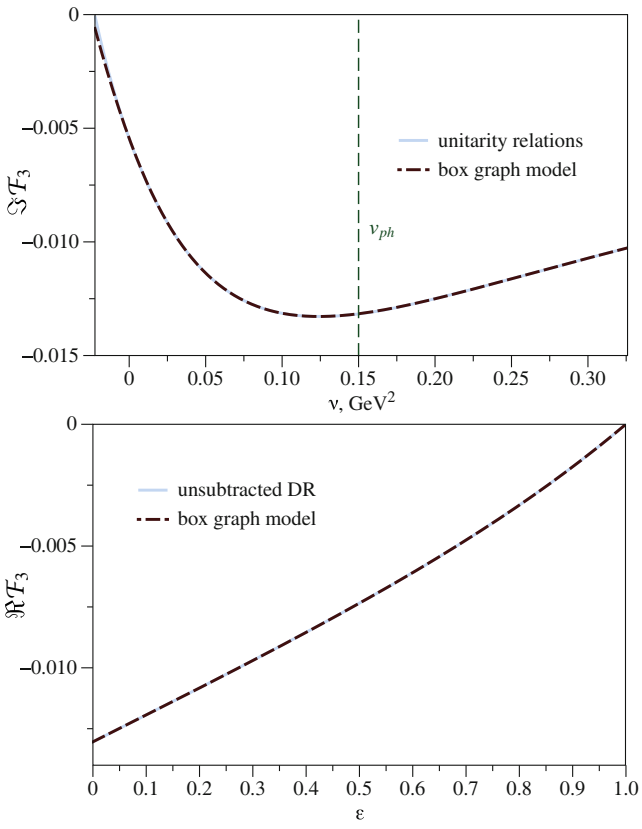

Fig. 17. Same as fig. 15, but for the structure amplitude $\mathcal{F}_3$.

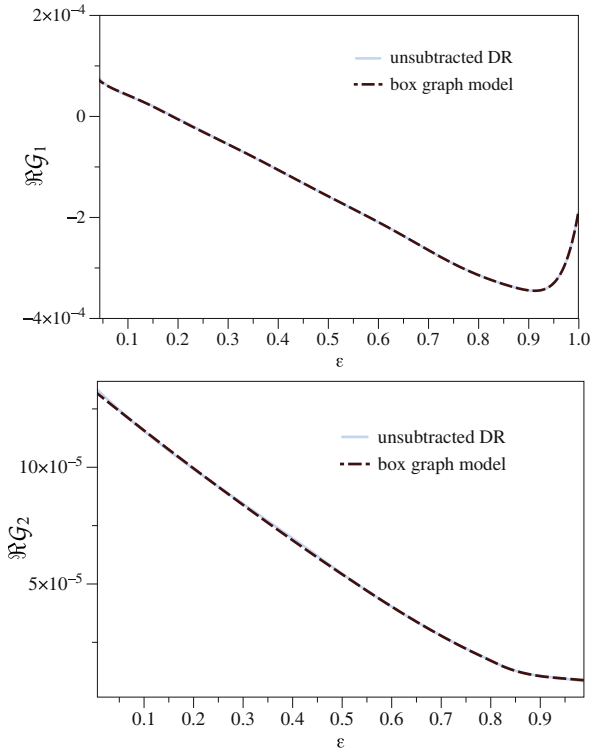

Fig. 18. ε dependence of the real part of the structure amplitudes $\mathcal{G}_1$, $\mathcal{G}_2$ in case of the F_2F_2 vertex structure with dipole FFs for $Q^2 = 0.1\,\mathrm{GeV}^2$.

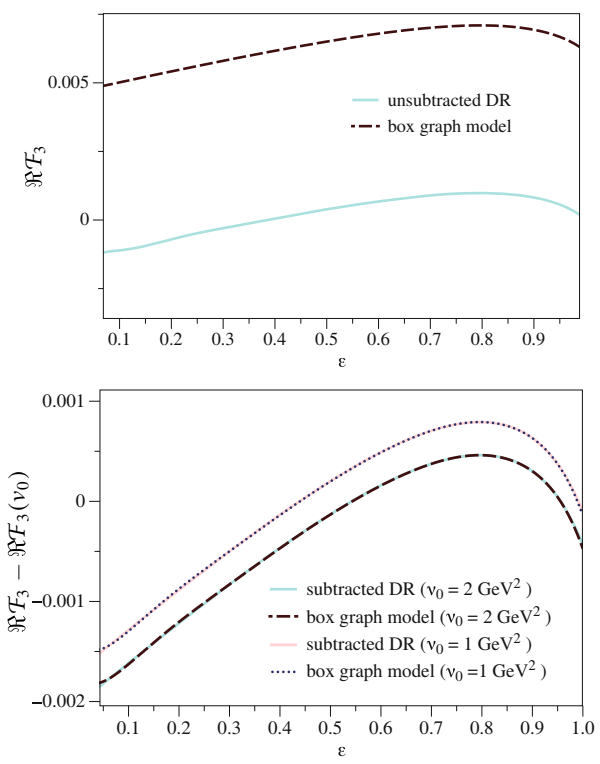

Fig. 19. ε dependence of the real part of the structure amplitude $\mathcal{F}_3$ in case of the F_2F_2 vertex structure with dipole FFs for $Q^2 = 0.1\,\mathrm{GeV}^2$. Upper panel: comparison of the box diagram evaluation with unsubtracted DR. Lower panel: comparison between the box diagram and DR evaluations when performing one subtraction. The calculations are shown for two different subtraction points: $\nu_0 = 1\,\mathrm{GeV}^2$, and $\nu_0 = 2\,\mathrm{GeV}^2$.

agram evaluation for F_1F_1 vertex structure of the real parts (for the sum of direct and crossed box diagrams), we see from figs. 15–17 that they nicely agree over the whole physical region of the parameter ε, which is related to ν as

$$\nu = \sqrt{\frac{1+\varepsilon}{1-\varepsilon}}\nu_{ph}, \tag{53}$$

with ν_{ph} defined in eq. (26). We checked that in case of the F_1F_2 vertex structure, the real parts as obtained from the box diagram model calculation also agree with the unsubtracted DR results. In case of the F_2F_2 vertex structure, the unsubtracted DRs reproduce the box diagram model results for the amplitudes $\mathcal{F}_2$, $\mathcal{G}_1$, $\mathcal{G}_2$ for both FF models. As an example, we show the results for $\mathcal{G}_1$ and $\mathcal{G}_2$ in fig. 18. These amplitudes are UV finite in case of the point-like model calculation. The real part of the $\mathcal{F}_3$ amplitude requires an UV regularization for the point-like box graph model. Consequently the DR for the amplitude $\mathcal{F}_3$ requires one subtraction. The resulting subtraction term cannot be reconstructed from the imaginary part of the amplitude $\mathcal{F}_3$. This term describes the contribution of physics at high energies to low-energy processes. When using dipole FFs for the F_2F_2 vertex structure, one finds that the unsubtracted DR for the elastic contributions also converges for $\mathcal{F}_3$. The results for the real part of the structure amplitude $\mathcal{F}_3$ for the case of the F_2F_2 vertex structure are shown in fig. 19. One firstly noticed from fig. 19 (left panel) that the calculated real part of $\mathcal{F}_3$ in the box graph model does not agree with the amplitude reconstructed using unsubtracted DRs. Although the box diagram calculation for $\mathcal{F}_3$ is convergent for the F_2F_2 vertex structure when using on-shell vertices with dipole FFs, we like to stress that this result is model dependent. We notice however that after performing one subtraction, we find an agreement between the DR calculation and the box diagram model evaluation, see right panel of fig. 19. Even though numerically the Feynman diagram calculation may yield satisfactory results over some kinematic range, as will be shown in the following, fixing the subtraction function to reproduce the Feynman diagram calculation with effective vertices would be a model dependent assumption, and is not a consequence of quantum field theory.

As a first step, we will fix the subtraction function in the following to empirical TPE data, with the assumption of only the nucleon intermediate state contribution. A fully consistent application of the DR formalism will require also to add the inelastic term, and then fit the subtraction term to the data. Such inclusion of inelastic states is beyond the scope of the present work.

To test the numerical convergence for different kinematical situations, we show in fig. 20 the contributions to the real parts of $\mathcal{G}_1$, $\mathcal{G}_2$, and $\mathcal{F}_3$ evaluated through unsubtracted DRs, as function of the upper integration limit in the DRs. We see from fig. 20 that for the case

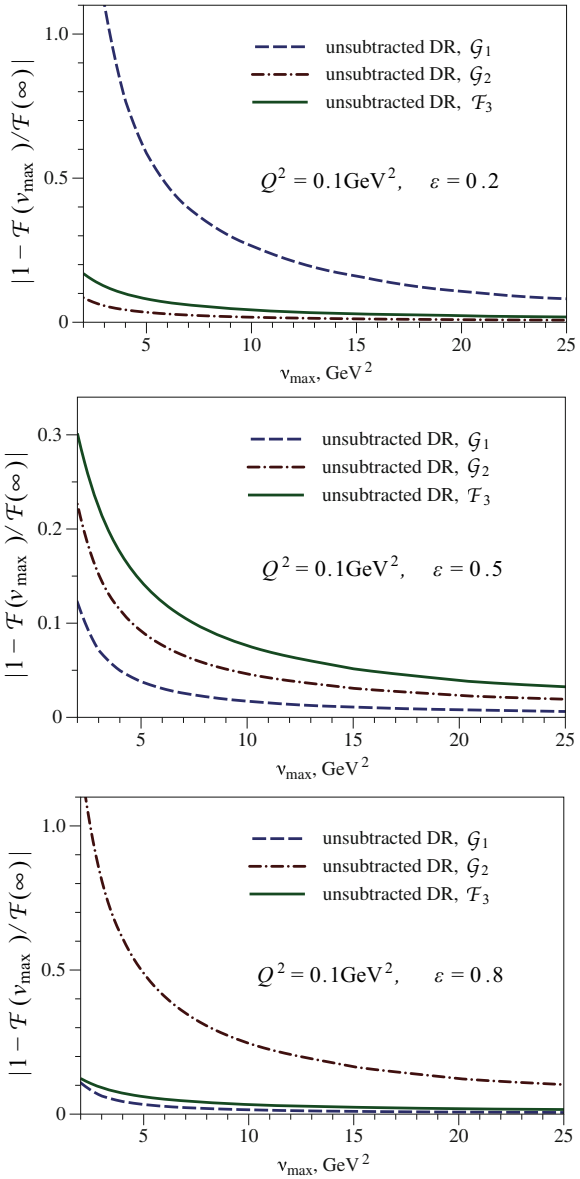

Fig. 20. Real parts of $\mathcal{G}_1$, $\mathcal{G}_2$, and $\mathcal{F}_3$ evaluated through unsubtracted DRs, as function of the upper integration limit $\nu_{\max}$. The plot shows the relative deviation for each amplitude from its value for $\nu_{\max} = \infty$, denoted by $\mathcal{F}(\infty)$, where $\mathcal{F}$ stands for $\mathcal{G}_1$, $\mathcal{G}_2$, $\mathcal{F}_3$. All results are for the F_2F_2 vertex structure with dipole FFs.

of the F_2F_2 vertex structure with dipole FFs, the convergence of unsubtracted DRs is slowest at large (small) values of ε for $\mathcal{G}_2$ ($\mathcal{G}_1$), respectively, while at intermediate values of ε the slowest convergence occurs for $\mathcal{F}_3$. For a phenomenological evaluation of the TPE contribution to elastic electron-nucleon scattering, we like to minimize any model dependence due to higher energy contributions. In a full calculation, such contributions arise from inelastic states which always will require some approximate treatment. To minimize any such uncertainties and to provide a more flexible formalism when applied to data, we propose to consider a DR formalism with one subtraction for the amplitude $\mathcal{F}_3$. The subtraction constant will be obtained by a fit to elastic electron-nucleon scattering observables, in the region where precise data are available.

We next discuss the implementation of such a subtracted DR formalism for the TPE contribution and provide a detailed comparison to different observables. The TPE correction to the unpolarized elastic electron-proton scattering cross section in eq. (14) can be expressed as the sum of a term evaluated using an unsubtracted DR and a term arising from the F_2F_2 contribution of $\mathcal{F}_3$, which we will evaluate by performing a subtraction:

$$\delta_{2\gamma} = \delta^0_{2\gamma} + f(\nu, Q^2)\Re\mathcal{F}_3^{F_2F_2}, \tag{54}$$

with

$$\delta^0_{2\gamma} = \frac{2}{G_M^2 + \frac{\varepsilon}{\tau}G_E^2}\left(G_M(\varepsilon - 1)\frac{\nu}{M^2}\Re\mathcal{F}_3^{F_1F_1+F_1F_2} + G_M\Re\mathcal{G}_1 + \frac{\varepsilon}{\tau}G_E\Re\mathcal{G}_2\right), \tag{55}$$

and

$$f(\nu, Q^2) = \frac{2G_M(\varepsilon - 1)}{G_M^2 + \frac{\varepsilon}{\tau}G_E^2}\frac{\nu}{M^2}\,. \tag{56}$$

The polarization transfer observables of eqs. (15) and (16) can also be expressed as model-independent terms $(\frac{P_t}{P_l})^0$, $(\frac{P_l}{P_l^{\text{Born}}})^0$ and the contribution due to $\mathcal{F}_3^{F_2F_2}$ as

$$\frac{P_t}{P_l} = \left(\frac{P_t}{P_l}\right)^0 + g(\nu, Q^2)\Re\mathcal{F}_3^{F_2F_2}, \tag{57}$$

$$\frac{P_l}{P_l^{\text{Born}}} = \left(\frac{P_l}{P_l^{\text{Born}}}\right)^0 + h(\nu, Q^2)\Re\mathcal{F}_3^{F_2F_2}, \tag{58}$$

with

$$g(\nu, Q^2) = -\sqrt{\frac{2\varepsilon}{\tau(1+\varepsilon)}}\frac{1-\varepsilon}{1+\varepsilon}\frac{G_E}{G_M^2}\frac{\nu}{M^2}\,, \tag{59}$$

$$h(\nu, Q^2) = -\frac{2\varepsilon}{\tau G_M^2 + \varepsilon G_E^2}\frac{1}{G_M}\frac{\varepsilon\tau G_M^2 + G_E^2}{1+\varepsilon}\frac{\nu}{M^2}\,. \tag{60}$$

The predictions for the elastic electron-proton scattering observables can be made with one subtraction point at $\nu = \nu_0$, which we express as

$$\delta_{2\gamma}(\nu, Q^2) = f(\nu, Q^2)\left[\Re\mathcal{F}_3^{F_2F_2}(\nu, Q^2) - \Re\mathcal{F}_3^{F_2F_2}(\nu_0, Q^2)\right] + \delta^0_{2\gamma}(\nu, Q^2) + f(\nu, Q^2)\,\Re\mathcal{F}_3^{F_2F_2}(\nu_0, Q^2), \tag{61}$$

where we can express the value of subtraction function $\Re\mathcal{F}_3^{F_2F_2}(\nu_0, Q^2)$ through $\delta_{2\gamma}(\nu_0, Q^2)$, which has to be obtained from experiment, as

$$\Re\mathcal{F}_3^{F_2F_2}(\nu_0, Q^2) = \frac{\delta_{2\gamma}(\nu_0, Q^2) - \delta^0_{2\gamma}(\nu_0, Q^2)}{f(\nu_0, Q^2)}\,. \tag{62}$$

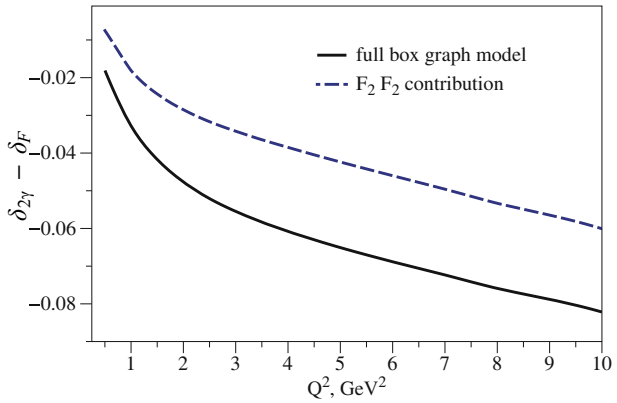

Fig. 21. Model prediction for the TPE correction $\delta_{2\gamma} - \delta_F$, with δ_F is the Feshbach term of eq. (45), for $\varepsilon = 0.01$.

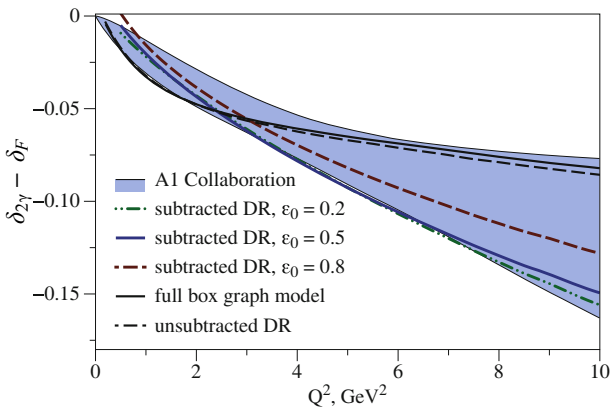

Fig. 22. Subtracted DR based prediction for the TPE corrections $\delta_{2\gamma} - \delta_F$, in comparison with the box diagram model prediction, unsubtracted DR prediction, for $\varepsilon = 0.01$, and with the parametrization of experimental data [2], for $\varepsilon = 0$ (blue band). The subtracted DR predictions are shown for three choices of the subtraction point: $\varepsilon_0 = 0.2,\ 0.5,\ 0.8$.

We can then insert this subtraction term (for every fixed value of Q^2) into eqs. (57) and (58) and make predictions for the ν or ϵ dependence of these observables as

$$\left(\frac{P_t}{P_l}\right)(\nu,Q^2) = \left(\frac{P_t}{P_l}\right)^0(\nu,Q^2) + g(\nu,Q^2) \times \left[\Re\mathcal{F}_3^{F_2F_2}(\nu,Q^2) - \Re\mathcal{F}_3^{F_2F_2}(\nu_0,Q^2)\right] + g(\nu,Q^2)\frac{\delta_{2\gamma}(\nu_0,Q^2) - \delta^0_{2\gamma}(\nu_0,Q^2)}{f(\nu_0,Q^2)}, \tag{63}$$

$$\left(\frac{P_l}{P_l^{\rm Born}}\right)(\nu,Q^2) = \left(\frac{P_l}{P_l^{\rm Born}}\right)^0(\nu,Q^2) + h(\nu,Q^2) \times \left[\Re\mathcal{F}_3^{F_2F_2}(\nu,Q^2) - \Re\mathcal{F}_3^{F_2F_2}(\nu_0,Q^2)\right] + h(\nu,Q^2)\frac{\delta_{2\gamma}(\nu_0,Q^2) - \delta^0_{2\gamma}(\nu_0,Q^2)}{f(\nu_0,Q^2)}. \tag{64}$$

In eqs. (61), (63) and (64) the difference $\Re\mathcal{F}_3^{F_2F_2}(\nu,Q^2) - \Re\mathcal{F}_3^{F_2F_2}(\nu_0,Q^2)$ is calculated from a subtracted DR. In the following, we determine the subtraction term from the unpolarized cross section measurements [2], and show our predictions for the different observables. The TPE correction to the unpolarized elastic electron-proton scattering evaluated in the model calculation of sect. 4, with the Feshbach term subtracted, is shown in fig. 21 for a small value of ε. It is seen from fig. 21 that the departure of the TPE correction from the Feshbach term strongly increases with increasing Q^2. One also sees that at larger Q^2, this is mainly due to the contribution from the F_2F_2 vertex structure.

To compare our DR results for the proton intermediate state contribution with the data, we perform, for every fixed value of Q^2, one subtraction for the amplitude $\mathcal{F}_3$ with the subtraction point fixed by one cross section result, which we take from ref. [2].

We like to caution that the two-parameter "empirical" extraction of ref. [2] is too simplified to be interpreted as "data". In order to obtain an empirical TPE extraction, one would have to apply a full dispersion formalism (elastic + inelastic) and provide a fit of the subtraction function directly to the elastic scattering observables. The present work is a first necessary step towards this aim. Any comparison with the simplified TPE extraction in ref. [2] which we give in the following should therefore only be considered as qualitative.

For comparison, we also show the result for the box diagram model in fig. 22. The difference between the results for different choices of the subtraction point corresponds to the uncertainty of our procedure. We would like to notice that for Q^2 larger than around $1\,\mathrm{GeV}^2$ the account of inelastic intermediate states becomes increasingly important. Also a description in terms of intermediate hadronic states ceases to be valid for large momentum transfer: due to the scattering off individual quarks, one will go over into a partonic picture [12,13,18,19,24].

We next discuss in more detail the TPE evaluations using nucleon intermediate state only in the region of low momentum transfers, to test the validity of this approximation. The TPE correction to the unpolarized elastic electron-proton scattering evaluated in the box diagram model of sect. 4 is shown in fig. 23 as a function of ε for momentum transfers $Q^2 = 0.05\,\mathrm{GeV}^2$ and $Q^2 = 1\,\mathrm{GeV}^2$. Our model calculation results are in agreement with a similar calculation performed by Blunden, Melnitchouk and Tjon [9]. For small momentum transfers, the model calculation approaches the Feshbach limit, and is in agreement with the experimental results.

We next show our predictions at low momentum transfers based on the subtracted DR framework. As seen from fig. 24, the subtracted DR result describes the data better in the region of intermediate ε. For higher ε values, *i.e.*, higher energies, the contribution of inelastic intermediate states become important and the agreement between theory and experiment becomes worse. One also notices clear deviations at lower values of ε. This may arise due to the assumption in the experimental TPE analysis of a linear ε-behavior for the difference $\delta_{2\gamma} - \delta_F$. The theoretical calculations show non-linear behaviour in ε for this region.

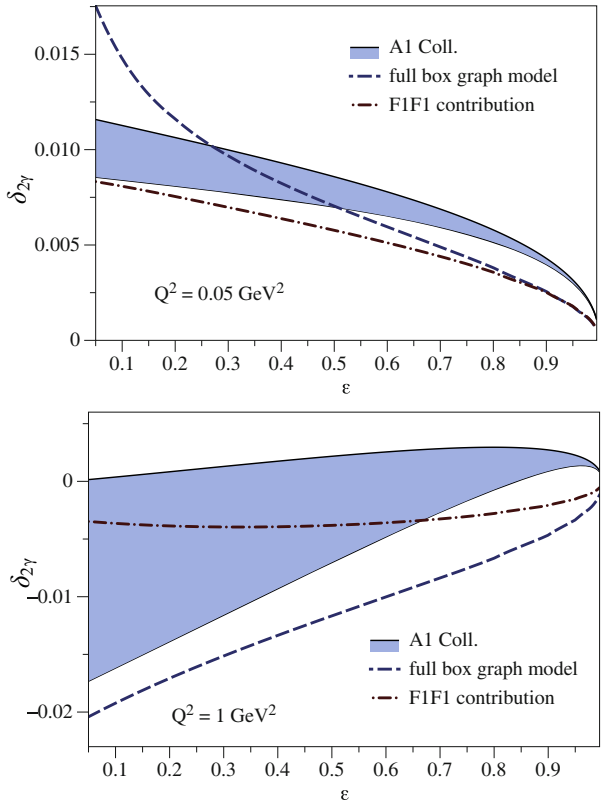

Fig. 23. Model prediction for the TPE correction for $Q^2 = 0.05\,\mathrm{GeV}^2$ (upper panel) and $Q^2 = 1\,\mathrm{GeV}^2$ (lower panel). Dashed curve: full box diagram model result; dash-dotted curve: F_1F_1 vertex contribution only. The experimental results from the MAMI/A1 Collaboration [2] are shown by the blue bands.

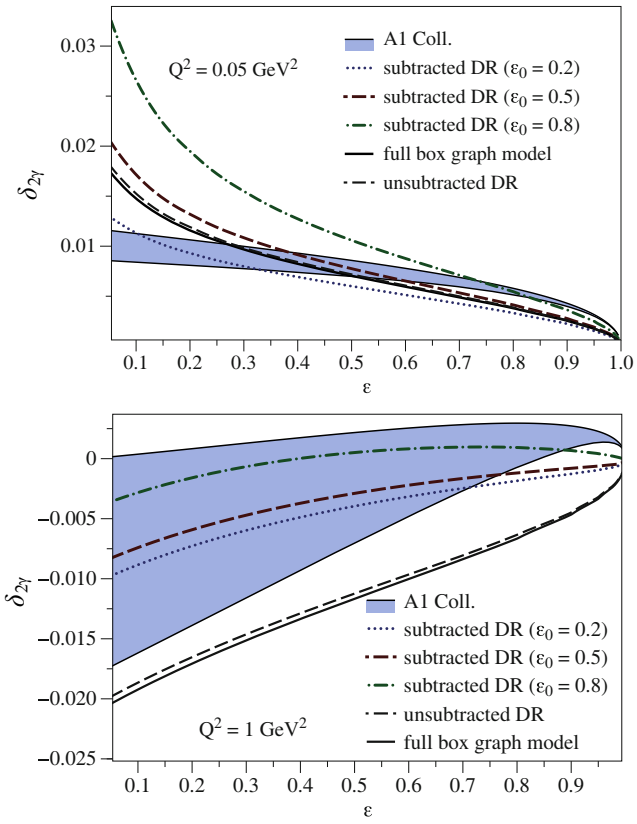

Fig. 24. Subtracted DR based predictions for the TPE corrections for $Q^2 = 0.05\,\mathrm{GeV}^2$ (upper panel) and $Q^2 = 1\,\mathrm{GeV}^2$ (lower panel), in comparison with the unsubtracted DR prediction as well as with the box diagram model. The subtracted DR curves correspond with three choices for the subtraction points: $\varepsilon_0 = 0.2, 0.5, 0.8$. The blue bands correspond with the experimental result from the fit of ref. [2].

For $Q^2 \approx 0.206\,\mathrm{GeV}^2$, the CLAS Collaboration has recently performed measurements of the ratio of e^+p to e^-p elastic scattering cross section [29]. Its deviation from unity is directly related to the TPE corrections. Furthermore, the ratio P_t/P_l was measured for momentum transfer values $Q^2 = 0.298\,\mathrm{GeV}^2$ [57] and $Q^2 = 0.308\,\mathrm{GeV}^2$ [58] in Hall A of JLab. In figs. 25 and 26 we show the theoretical estimates for physical observables based on the subtracted DR prediction. We fix the subtracted amplitude $\mathcal{F}_3$ according to eq. (62), by using the unpolarized cross section analysis of ref. [2] at one point in ε as input. We choose the subtraction point $\varepsilon_0 = 0.83$, which is in the ε-range of both experiments. For both observables we use the FFs from the P_t/P_l measurement of ref. [57]. We extract the TPE correction $\delta_{2\gamma}$ from the CLAS data of the cross section ratio $R_{2\gamma} = \sigma(e^+p)/\sigma(e^-p)$ by $\delta_{2\gamma} \approx (1 + \delta_{\mathrm{even}}) \times (1 - R_{2\gamma})/2$, where $\delta_{\mathrm{even}} \approx -0.2$ is the total charge-even radiative correction factor according to ref. [29]. Note that for the CLAS data, which have been radiatively corrected according to the Mo and Tsai (MT) procedure [59] in ref. [29], we applied the correction $\delta^{\mathrm{MT}}_{2\gamma,\mathrm{soft}} - \delta^{\mathrm{MaTj}}_{2\gamma,\mathrm{soft}}$ to the data in order to compare relative to the Maximon and Tjon (MaTj) procedure which we follow in this paper. The bound on the subtracted DR analysis arises from the experimental uncertainty entering through the subtraction. We conclude from figs. 25 and 26 that all measurements are in agreement for small momentum transfers and the TPE corrections are described by the elastic contribution within the errors of the experiments.

We next discuss the polarization transfer observables for momentum transfer $Q^2 \approx 2.5\,\mathrm{GeV}^2$ where data have been taken both for P_t and P_l separately [27]. In our theoretical predictions, we use the 1γ-exchange FFs taken from the P_t/P_l ratio measurement. To evaluate the TPE structure amplitudes, we use the dipole FFs as an input. The comparison with the data for the ratio P_t/P_l is shown in fig. 27. As one sees, the present data for P_t/P_l [28] does not allow to extract a TPE effect, indicating a cancellation between the three TPE amplitudes for this specific observable. The comparison with the data [28] for the absolute polarization transfer observable P_l/P_l^{Born} [28] is also shown in fig. 27. It shows that the point at $\varepsilon = 0.635$ with $P_l/P_l^{\mathrm{Born}} = 1.007 \pm 0.005$ is consistent with the proton contribution only, but the point at $\varepsilon = 0.785$ with $P_l/P_l^{\mathrm{Born}} = 1.023 \pm 0.006$ requires further theoretical investigations, *e.g.*, account of inelastic intermediate states

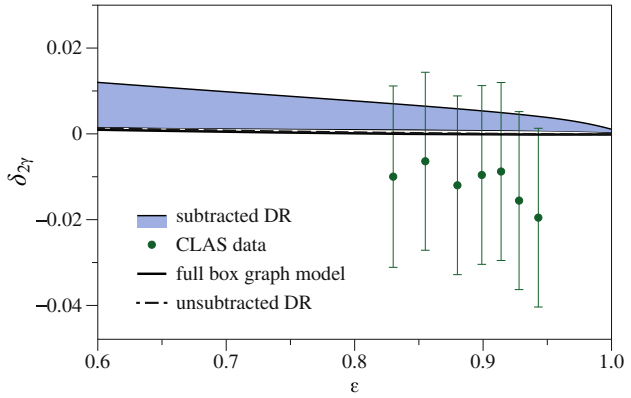

Fig. 25. Comparison of the subtracted DR prediction for the TPE correction for $Q^2 = 0.206\,\mathrm{GeV}^2$ with the data [29], with the unsubtracted DR prediction and with the box diagram model. The subtraction point used in the DR analysis is $\varepsilon_0 = 0.83$.

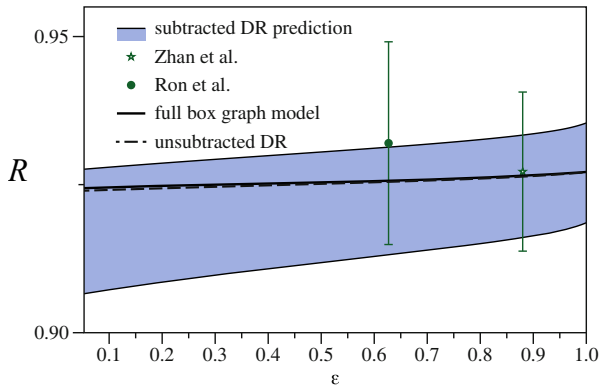

Fig. 26. Comparison of the subtracted DR prediction for the ratio $R = -\mu_p \sqrt{\frac{1+\varepsilon}{\varepsilon}\tau}\frac{P_t}{P_l}$ for $Q^2 = 0.298\,\mathrm{GeV}^2$ with the data [57,58], with the unsubtracted DR prediction and with the box diagram model. The subtraction point used in the DR analysis is $\varepsilon_0 = 0.83$.

which are relevant at these larger momentum transfers. The specific property of the subtracted DR analysis for the ratio P_l/P_l^{Born} is the divergence of the errors for $\varepsilon \to 1$ as $1/\sqrt{1-\varepsilon}$.

6 Conclusions and outlook

In this work we have studied the TPE corrections to elastic electron-proton scattering with the aim to minimize the model dependence when applied to data. For this purpose we have studied a subtracted dispersion relation formalism where the real part of the $\mathcal{F}_3$ structure amplitude is reconstructed from the corresponding imaginary parts through a subtracted dispersion relation. We have related the subtraction constant at a fixed value of Q^2 to a precisely measured cross section point at one value of ε. The remaining ε dependence of the cross section, as well as the other observables then follow as predictions in our formalism. In this work, we have tested this formalism on the elastic, *i.e.* proton intermediate state, TPE contribution.

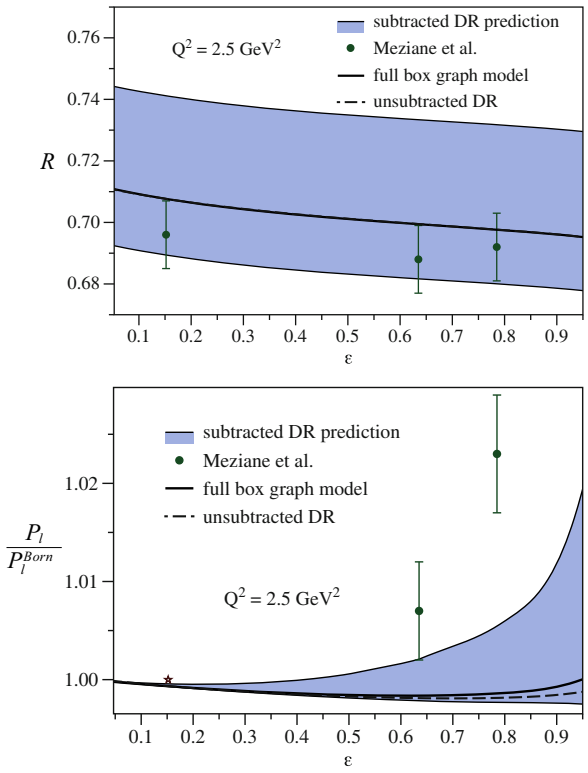

Fig. 27. Comparison of the subtracted DR predictions for the ratio $R = -\mu_p \sqrt{\frac{1+\varepsilon}{\varepsilon}\tau}\frac{P_t}{P_l}$ (upper panel) and P_l/P_l^{Born} (lower panel) for $Q^2 = 2.5\,\mathrm{GeV}^2$ with the data of ref. [28], with the unsubtracted DR prediction and with the box diagram model. The subtraction point used in the DR analysis is $\varepsilon_0 = 0.785$.

We have made a detailed comparison with existing data. In the low momentum transfer region, where the nucleon intermediate state contribution is expected to dominate, the presented formalism provides a flexible framework to provide a more accurate extraction of the TPE correction to elastic electron-nucleon scattering. At larger values of Q^2, the presented subtracted dispersion relation formalism can be extended in a next step to include inelastic intermediate state contributions. Moreover, a further extension of the subtracted DR formalism is to evaluate the TPE corrections for the case of muon-proton scattering at low energies, which requires the inclusion of lepton-mass correction terms. A first step in this direction was already performed [60].

We thank J. Bernauer for providing us with the details of the analysis of experimental data on TPE, C.E. Carlson, M. Gorchtein, N. Kivel, and V. Pascalutsa for technical support and useful discussions. This work was supported by the Deutsche Forschungsgemeinschaft DFG in part through the Collaborative Research Center (The Low-Energy Frontier of the Standard Model (SFB 1044)), in part through the Graduate School (Symmetry Breaking in Fundamental Interactions (DFG/GRK 1581)), and in part through the Cluster of Excellence (Precision Physics, Fundamental Interactions and Structure of Matter (PRISMA)).

Appendix A. Phases entering the unitarity relations

The unitarity relation phases entering Eq. (19) can be expressed in terms of the Mandelstam variables as

$$\begin{aligned}
\cos\phi' &= \frac{1}{\sqrt{4Q^2Q_1^2xx_1}x_2}\Big(-Q_2^2+Q^2x+Q_1^2x_1 \\
&\quad +\frac{sQ_2^2}{(s-M^2)^2}Q_2^2(xQ_1^2+x_1Q^2)\Big), \\
\cos\tilde{\phi} &= \frac{1}{\sqrt{4Q^2Q_2^2xx_2}}\left(xQ_2^2+x_2Q^2-Q_1^2\right), \\
\cos\tilde{\phi}' &= \frac{1}{\sqrt{4Q_1^2Q_2^2x_1x_2}}\left(-Q^2+x_2Q_1^2+x_1Q_2^2\right), \\
\cos(\phi-\phi') &= \frac{1}{2xx_1x_2}\Big(x^2+x_1^2+x_2^2-1 \\
&\quad +2\frac{s^3}{(s-M^2)^6}Q^2Q_1^2Q_2^2\Big), \\
\cos(\phi+\tilde{\phi}) &= \frac{1}{\sqrt{4x_1x_2Q_1^2Q_2^2}}\frac{1}{x}\Big(-Q_1^2x_1-Q_2^2x_2+Q^2 \\
&\quad -\frac{sQ^2}{(s-M^2)^2}(Q_2^2+Q_1^2)x\Big),
\end{aligned} \tag{A.1}$$

with

$$\begin{aligned}
x &\equiv \frac{1}{2}(1+\cos\theta_{\rm cm}) = 1-\frac{sQ^2}{(s-M^2)^2}\,, \\
x_1 &\equiv \frac{1}{2}(1+\cos\theta_1) = 1-\frac{sQ_1^2}{(s-M^2)^2}\,, \\
x_2 &\equiv \frac{1}{2}(1+\cos\theta_2) = 1-\frac{sQ_2^2}{(s-M^2)^2}\,.
\end{aligned} \tag{A.2}$$

Appendix B. Different integration coordinates in unitarity relations

The boundaries of the ellipse mentioned in sect. 3.3 correspond to $\cos^2\phi_1 = 0$. Defining $z_1 \equiv \cos\theta_1$, $z_2 \equiv \cos\theta_2$, $z \equiv \cos\theta_{\rm cm}$ the ellipse equation is given by

$$1-z^2-z_1^2-z_2^2 = -2zz_1z_2, \tag{B.1}$$

The coordinates z_1, z_2 can be rotated by 45°, so that the new coordinate system coincides with the axes of the ellipse

$$\tilde{z}_1 = -\frac{1}{\sqrt{2}}(z_1+z_2), \qquad \tilde{z}_2 = \frac{1}{\sqrt{2}}(z_1-z_2). \tag{B.2}$$

The $\tilde{z}_2$-axis corresponds to the line $Q_1^2 = Q_2^2$, whereas the $\tilde{z}_1$-axis corresponds to the line $Q_2^2 = Q_{\rm max}^2 - Q_1^2$. The phase space integration in terms of new coordinates is expressed as

$$\int {\rm d}\Omega = 2\int_{-1}^{1}{\rm d}\cos\theta_1\int_0^{\pi}{\rm d}\phi_1 = \int\frac{{\rm d}\tilde{z}_1\,{\rm d}\tilde{z}_2}{\sqrt{1-z^2}}\frac{2}{|\alpha|}\,, \tag{B.3}$$

with $\alpha \equiv \sin\theta_1\sin\phi_1$. The ellipse equation is then given by

$$\frac{\tilde{z}_1^2}{1+z}+\frac{\tilde{z}_2^2}{1-z} = 1. \tag{B.4}$$

The integration of eq. (B.3) maps out the whole surface of the ellipse. It is therefore convenient to introduce the elliptic coordinates α, ϕ as

$$\begin{aligned}
\tilde{z}_1 &= \sqrt{1-\alpha^2}\sqrt{1+z}\cos(\phi), \\
\tilde{z}_2 &= \sqrt{1-\alpha^2}\sqrt{1-z}\sin(\phi),
\end{aligned} \tag{B.5}$$

which satisfy

$$\frac{\tilde{z}_1^2}{1+z}+\frac{\tilde{z}_2^2}{1-z} = 1-\alpha^2. \tag{B.6}$$

The photons virtualities Q_1^2, Q_2^2 are symmetric in terms of the elliptic coordinates α, ϕ. The phase space integration in terms of these elliptic coordinates can then be expressed as

$$\int {\rm d}\Omega = \frac{2}{\sqrt{1-z^2}}\int {\rm d}\tilde{z}_1\,{\rm d}\tilde{z}_2\frac{1}{|\alpha|} = 2\int_0^1{\rm d}\alpha\int_0^{2\pi}{\rm d}\phi. \tag{B.7}$$

References

1. A1 Collaboration (J.C. Bernauer *et al.*), Phys. Rev. Lett. **105**, 242001 (2010) arXiv:1007.5076 [nucl-ex].
2. A1 Collaboration (J.C. Bernauer *et al.*), Phys. Rev. C **90**, 015206 (2014) arXiv:1307.6227 [nucl-ex].
3. C.F. Perdrisat, V. Punjabi, M. Vanderhaeghen, Prog. Part. Nucl. Phys. **59**, 694 (2007) hep-ph/0612014.
4. Jefferson Lab Hall A Collaboration (M.K. Jones *et al.*), Phys. Rev. Lett. **84**, 1398 (2000) nucl-ex/9910005.
5. Jefferson Lab Hall A Collaboration (O. Gayou *et al.*), Phys. Rev. Lett. **88**, 092301 (2002) nucl-ex/0111010.
6. V. Punjabi, C.F. Perdrisat, K.A. Aniol, F.T. Baker, J. Berthot, P.Y. Bertin, W. Bertozzi, A. Besson *et al.*, Phys. Rev. C **71**, 055202 (2005) **71**, 069902(E) (2005) nucl-ex/0501018.
7. A.J.R. Puckett, E.J. Brash, M.K. Jones, W. Luo, M. Meziane, L. Pentchev, C.F. Perdrisat, V. Punjabi *et al.*, Phys. Rev. Lett. **104**, 242301 (2010) arXiv:1005.3419 [nucl-ex].
8. V. Punjabi, Phys. Part. Nucl. **45**, 163 (2014).
9. P.G. Blunden, W. Melnitchouk, J.A. Tjon, Phys. Rev. Lett. **91**, 142304 (2003) nucl-th/0306076.
10. P.A.M. Guichon, M. Vanderhaeghen, Phys. Rev. Lett. **91**, 142303 (2003) hep-ph/0306007.
11. C.E. Carlson, M. Vanderhaeghen, Ann. Rev. Nucl. Part. Sci. **57**, 171 (2007) hep-ph/0701272.
12. Y.C. Chen, A. Afanasev, S.J. Brodsky, C.E. Carlson, M. Vanderhaeghen, Phys. Rev. Lett. **93**, 122301 (2004) hep-ph/0403058.
13. A.V. Afanasev, S.J. Brodsky, C.E. Carlson, Y.C. Chen, M. Vanderhaeghen, Phys. Rev. D **72**, 013008 (2005) hep-ph/0502013.

14. P.G. Blunden, W. Melnitchouk, J.A. Tjon, Phys. Rev. C **72**, 034612 (2005) nucl-th/0506039.
15. M. Gorchtein, Phys. Lett. B **644**, 322 (2007) hep-ph/0610378.
16. D. Borisyuk, A. Kobushkin, Phys. Rev. C **78**, 025208 (2008) arXiv:0804.4128 [nucl-th].
17. D. Borisyuk, A. Kobushkin, Phys. Rev. D **79**, 034001 (2009) arXiv:0811.0266 [hep-ph].
18. N. Kivel, M. Vanderhaeghen, Phys. Rev. Lett. **103**, 092004 (2009) arXiv:0905.0282 [hep-ph].
19. N. Kivel, M. Vanderhaeghen, JHEP **04**, 029 (2013) arXiv:1212.0683 [hep-ph].
20. K.M. Graczyk, Phys. Rev. C **88**, 065205 (2013) arXiv:1306.5991 [hep-ph].
21. D. Borisyuk, A. Kobushkin, Phys. Rev. C **89**, 025204 (2014) arXiv:1306.4951 [hep-ph].
22. J. Arrington, W. Melnitchouk, J.A. Tjon, Phys. Rev. C **76**, 035205 (2007) arXiv:0707.1861 [nucl-ex].
23. Y.C. Chen, C.W. Kao, S.N. Yang, Phys. Lett. B **652**, 269 (2007) nucl-th/0703017.
24. D. Borisyuk, A. Kobushkin, Phys. Rev. C **76**, 022201 (2007) hep-ph/0703220 [HEP-PH].
25. M.A. Belushkin, H.-W. Hammer, U.-G. Meissner, Phys. Lett. B **658**, 138 (2008) arXiv:0705.3385 [hep-ph].
26. I.A. Qattan, A. Alsaad, J. Arrington, Phys. Rev. C **84**, 054317 (2011) arXiv:1109.1441 [nucl-ex].
27. J. Guttmann, N. Kivel, M. Meziane, M. Vanderhaeghen, Eur. Phys. J. A **47**, 77 (2011) arXiv:1012.0564 [hep-ph].
28. GEp2gamma Collaboration (M. Meziane *et al.*), Phys. Rev. Lett. **106**, 132501 (2011) arXiv:1012.0339 [nucl-ex].
29. CLAS Collaboration (M. Moteabbed *et al.*), Phys. Rev. C **88**, 025210 (2013) arXiv:1306.2286 [nucl-ex].
30. A.V. Gramolin, J. Arrington, L.M. Barkov, V.F. Dmitriev, V.V. Gauzshtein, R.A. Golovin, R.J. Holt, V.V. Kaminsky *et al.*, Nucl. Phys. Proc. Suppl. **225-227**, 216 (2012) arXiv:1112.5369 [nucl-ex].
31. OLYMPUS Collaboration (R. Milner *et al.*), Nucl. Instrum. Meth. A **741**, 1 (2014) arXiv:1312.1730 [physics.ins-det].
32. A. Antognini, F. Kottmann, F. Biraben, P. Indelicato, F. Nez, R. Pohl, Ann. Phys. **331**, 127 (2013) arXiv:1208.2637 [physics.atom-ph].
33. R. Pohl, A. Antognini, F. Nez, F.D. Amaro, F. Biraben, J.M.R. Cardoso, D.S. Covita, A. Dax *et al.*, Nature **466**, 213 (2010).
34. A. Antognini, F. Nez, K. Schuhmann, F.D. Amaro, FrancoisBiraben, J.M.R. Cardoso, D.S. Covita, A. Dax *et al.*, Science **339**, 417 (2013).
35. R. Pohl, R. Gilman, G.A. Miller, K. Pachucki, Annu. Rev. Nucl. Part. Sci. **63**, 175 (2013) arXiv:1301.0905 [physics.atom-ph].
36. J.C. Bernauer, R. Pohl, Sci. Am. **310**, 18 (2014).
37. K. Pachucki, Phys. Rev. A **53**, 2092 (1996).
38. A.P. Martynenko, Phys. At. Nucl. **69**, 1309 (2006) hep-ph/0509236.
39. C.E. Carlson, M. Vanderhaeghen, Phys. Rev. A **84**, 020102 (2011) arXiv:1101.5965 [hep-ph].
40. M. Gorchtein, F.J. Llanes-Estrada, A.P. Szczepaniak, Phys. Rev. A **87**, 052501 (2013) arXiv:1302.2807 [nucl-th].
41. R.J. Hill, G. Paz, Phys. Rev. Lett. **107**, 160402 (2011) arXiv:1103.4617 [hep-ph].
42. D. Nevado, A. Pineda, Phys. Rev. C **77**, 035202 (2008) arXiv:0712.1294 [hep-ph].
43. M.C. Birse, J.A. McGovern, Eur. Phys. J. A **48**, 120 (2012) arXiv:1206.3030 [hep-ph].
44. J.M. Alarcon, V. Lensky, V. Pascalutsa, Eur. Phys. J. C **74**, 2852 (2014) arXiv:1312.1219 [hep-ph].
45. C. Peset, A. Pineda, arXiv:1406.4524 [hep-ph].
46. W.A. McKinley, H. Feshbach, Phys. Rev. **74**, 1759 (1948).
47. P.G. Blunden, I. Sick, Phys. Rev. C **72**, 057601 (2005) nucl-th/0508037.
48. M. Jacob, G.C. Wick, Ann. Phys. **7**, 404 (1959) (Ann. Phys. **281**, 774 (2000)).
49. B. Pasquini, M. Vanderhaeghen, Phys. Rev. C **70**, 045206 (2004) hep-ph/0405303.
50. P. Van Nieuwenhuizen, Nucl. Phys. B **28**, 429 (1971).
51. T. Hahn, Nucl. Phys. Proc. Suppl. **89**, 231 (2000) hep-ph/0005029.
52. G.J. van Oldenborgh, J.A.M. Vermaseren, Z. Phys. C **46**, 425 (1990).
53. L.C. Maximon, J.A. Tjon, Phys. Rev. C **62**, 054320 (2000) nucl-th/0002058.
54. A. De Rujula, J.M. Kaplan, E. De Rafael, Nucl. Phys. B **35**, 365 (1971).
55. R.W. Brown, Phys. Rev. D **1**, 1432 (1970).
56. M. Gorchtein, Phys. Rev. C **90**, 052201 (2014) arXiv:1406.1612 [nucl-th].
57. X. Zhan, K. Allada, D.S. Armstrong, J. Arrington, W. Bertozzi, W. Boeglin, J.-P. Chen, K. Chirapatpimol *et al.*, Phys. Lett. B **705**, 59 (2011) arXiv:1102.0318 [nucl-ex].
58. Jefferson Lab Hall A Collaboration (G. Ron *et al.*), Phys. Rev. C **84**, 055204 (2011) arXiv:1103.5784 [nucl-ex].
59. L.W. Mo, Y.S. Tsai, Rev. Mod. Phys. **41**, 205 (1969).
60. O. Tomalak, M. Vanderhaeghen, Phys. Rev. D **90**, 013006 (2014) arXiv:1405.1600 [hep-ph].